An Analysis of Gravity Wave Spectral Characteristics in Moist Baroclinic Jet–Front Systems

JUNHONG WEI

Department of Meteorology, The Pennsylvania State University, University Park, Pennsylvania, and National Center for Atmospheric Research, Boulder, Colorado

FUQING ZHANG

Department of Meteorology, and Center for Advanced Data Assimilation and Predictability Techniques, The Pennsylvania State University, University Park, Pennsylvania

JADWIGA H. RICHTER

National Center for Atmospheric Research, Boulder, Colorado

ABSTRACT

This study investigates gravity wave spectral characteristics based on high-resolution mesoscale simulations of idealized moist baroclinic jet–front systems with varying degrees of convective instability, with the intent of improving nonorographic gravity wave parameterizations. In all experiments, there is a clear dominance of negative vertical flux of zonal momentum. The westward momentum flux is distributed around the estimated ground-based baroclinic wave phase velocity along the zonal direction, while strong moist runs indicate a dipole structure pattern with stronger westward momentum flux centers at slower phase velocity and weaker eastward momentum flux centers at faster phase velocity. The spectral properties of short-scale wave components (50–200 km) generally differ from those of medium-scale ones (200–600 km). Compared to the medium-scale wave components, the momentum flux phase speed spectra for the short-scale ones appear to be more sensitive to the increasing initial moisture content. The spectral behavior in horizontal wavenumber space or phase velocity space is highly anisotropic, with a noticeable preference along the jet direction, except for the short-scale components in strong moist runs. It is confirmed that the dry gravity wave source (i.e., upper jet and/or surface front) generates a relatively narrow and less symmetrical power spectrum (dominated by negative momentum flux) centered around lower phase velocity and horizontal wavenumber, whereas the moist gravity wave source (i.e., moist convection) generates a broader and more symmetrical power spectrum, with a broader range of phase speeds and horizontal wavenumbers. This study also shows that the properties of gravity wave momentum flux depend on the location relative to the baroclinic jet.

1. Introduction

Gravity waves are ubiquitous buoyancy oscillations in the atmosphere. The sources of gravity waves are sometimes categorized based on the presence or absence of topography. Orographic gravity waves are forced by flow over orography (e.g., Queney 1948; Smith 1980, 1990; Durran 1986, 1990, 2003). The main sources of nonorographic gravity waves include moist convection (e.g., Clark et al. 1986; Fovell et al. 1992; Alexander et al. 1995; Lane et al. 2001), atmospheric jets (e.g., Uccellini and Koch 1987; O'Sullivan and Dunkerton 1995; Zhang 2004), and frontal systems (Snyder et al. 1993; Griffiths and Reeder 1996). It is well established that gravity waves play an important role in a wide variety of atmospheric processes at possibly all scales. For example, gravity waves can initiate and organize convection (e.g., Zhang et al. 2001; Lane and Zhang 2011) and generate and modulate atmospheric turbulence (e.g., Shapiro 1980; Lane et al. 2004; Koch et al. 2005). Gravity waves can propagate over large distances from

Corresponding author address: Fuqing Zhang, Dept. of Meteorology, The Pennsylvania State University, 503 Walker Building, University Park, PA 16802.
E-mail: fzhang@psu.edu

their sources and transfer significant amounts of momentum, energy, and entropy to the mean flow, thereby contributing to the forcing of the circulation and the variability of the middle atmosphere (e.g., Holton 1982, 1983; Dunkerton and Butchart 1984; Andrews et al. 1987; Holton et al. 1995).

However, since the temporal and spatial scales of gravity waves are often too short to be fully captured in atmospheric general circulation models (GCMs), gravity wave parameterizations are needed to represent their effects on larger-scale flows (Fritts and Alexander 2003; Kim et al. 2003; Alexander et al. 2010), such as wave-induced forcing on the momentum. The Wentzel–Kramer–Brillouin (WKB) theory (Bretherton 1966; Grimshaw 1975; Müller 1976) has been the basis of many gravity wave parameterizations in GCMs (e.g., Lindzen 1981; Alexander and Dunkerton 1999; Warner and McIntyre 2001; Song and Chun 2008). Orographic gravity wave parameterizations have been emphasized for decades, and they are relatively well developed (e.g., Palmer et al. 1986; McFarlane 1987; Lott and Miller 1997; Lott 1999; Scinocca and McFarlane 2000; also see Stensrud 2007), while parameterizations of convective sources of gravity waves have become mature and begun to be implemented only in the last decade (e.g., Beres et al. 2004, 2005; Song and Chun 2005; Choi and Chun 2011). However, except for some limited experiments on the parameterizations of gravity waves from jets and fronts (e.g., Rind et al. 1988; Charron and Manzini 2002; Richter et al. 2010; de la Cámara and Lott 2015), parameterizations of gravity wave sources from jets and fronts remains a great challenge, and existing parameterizations use oversimplifications and tunable parameters as a result of poor physical understanding (Haynes 2005; Richter et al. 2010).

One way to better understand the jet/front gravity waves is to utilize idealized baroclinic wave simulations. See the recent review by Plougonven and Zhang (2014) on the current knowledge and understanding on gravity waves near jets and fronts. Most past idealized baroclinic wave experiments on gravity wave research primarily focused on a dry atmospheric process (e.g., O'Sullivan and Dunkerton 1995; Zhang 2004; Plougonven and Snyder 2005, 2007; Wang and Zhang 2007), which did not take moisture and heating into consideration. As an extension of the dry dynamics in Zhang (2004), Wei and Zhang (2014) recently performed a series of cloud-permitting simulations to study the characteristics and the dynamics of gravity waves in the moist baroclinic jet–front systems with varying degrees of convective instability. They demonstrated a much more energetic gravity wave field with increasingly higher initial moisture content.

These results are generally consistent with Waite and Snyder (2013) and Mirzaei et al. (2014). Note that many other studies have also highlighted the important role of moist processes in interacting with other dynamical processes to generate/maintain/amplify gravity waves (e.g., Koch and Dorian 1988; Zhang et al. 2001; Jewett et al. 2003; Plougonven et al. 2015). Furthermore, six groups of localized identifiable lower-stratospheric gravity waves were highlighted in Wei and Zhang (2014). Later, Wei and Zhang (2015) continued to investigate their propagating wave characteristics, source mechanisms, and wavenumber vector refraction budget based on a four-dimensional ray-tracing model. However, little is known about the characteristics of the gravity wave spectrum emanating from the jets/fronts under various moist conditions from those simulations in Wei and Zhang (2014), even though several localized wave examples have been relatively well studied. In particular, estimation of momentum fluxes, as well as their relationships with ground-based phase velocities, will be of great value to the community of gravity wave research in improving the nonorographic gravity wave drag parameterizations in GCMs (e.g., Preusse et al. 2014). Therefore, the aim of this paper, complementary to the previous work of Wei and Zhang (2014, 2015), is to explore the gravity wave spectral characteristics in moist baroclinic jet–front systems using high-resolution idealized simulations. The characteristics of momentum flux phase speed spectra have been documented by several studies on convective gravity waves (e.g., Kim and Chun 2010), as well as by one recent article based on dry idealized baroclinic waves (Kim et al. 2016). However, to the best of our knowledge, this is the first time for a study to provide a detailed presentation on the relationships between gravity wave momentum flux and phase velocity based on an ensemble of high-resolution idealized moist baroclinic jet–front systems for the purpose of improving the nonorographic gravity wave drag parameterizations.

This article is arranged as follows. A brief introduction to the data and method used for the work will be shown in section 2, followed in section 3 by the analysis of gravity wave momentum flux distribution in physical space. Section 4 will present the results on the wave spectrum in wavenumber space. The distribution of momentum fluxes in phase velocity space will be explored in section 5. Section 6 contains a summary.

2. Data and method

The data employed in this study come directly from the high-resolution idealized baroclinic wave experiments (10-km horizontal grid spacing and ~300-m
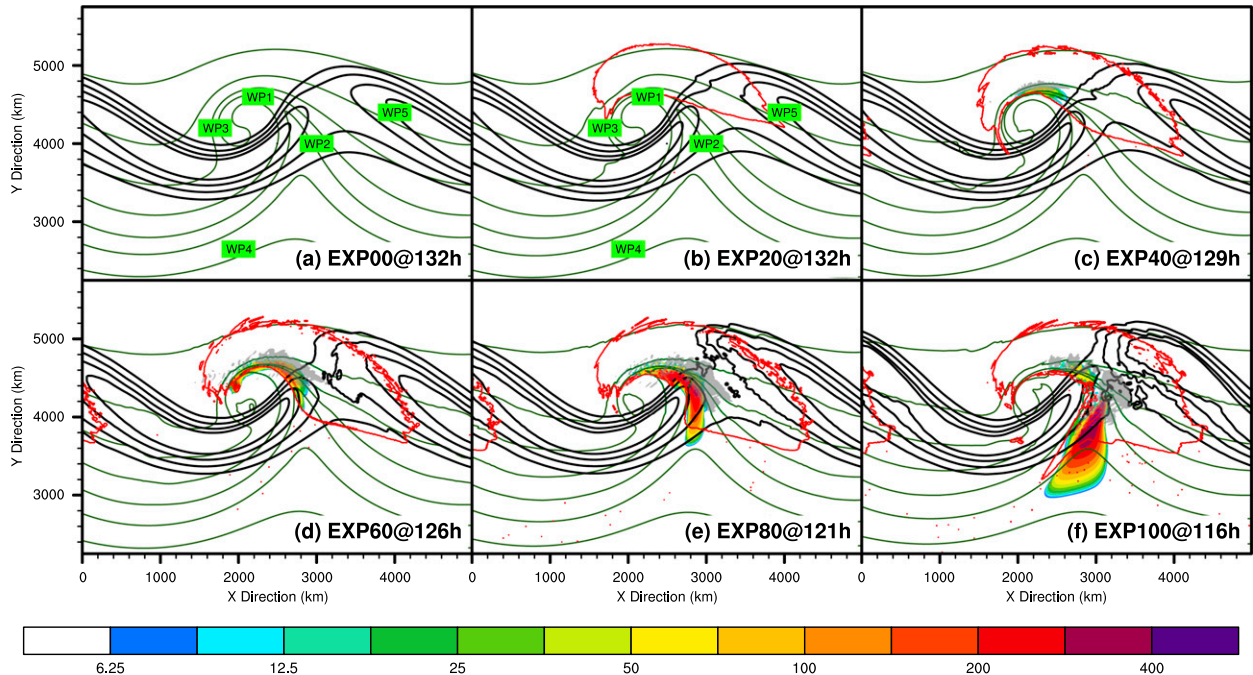
FIG. 1. The two-dimensional (x, y) space distribution of the maximum convective available potential energy (color fill; J kg^{-1}), the 1-h precipitation accumulation (gray shading for values greater than 1 mm), the vertically averaged positive-only latent heating rate (red lines; contours at 4.0×10^{-8} K s^{-1}), the temperature at 1-km altitude (dark green lines; contours at every 5 K), and the horizontal velocity magnitude at 8-km altitude (black lines; contours at 40, 45, 50, and 55 m s^{-1}) in (a) EXP00 at 132 h, (b) EXP20 at 132 h, (c) EXP40 at 129 h, (d) EXP60 at 126 h, (e) EXP80 at 121 h, and (f) EXP100 at 116 h. The abovementioned hours in EXP00–EXP100 are selected for the time when all the experiments share similar amplitudes of synoptic-scale atmospheric wind perturbations (also when the mature jet exit gravity waves emerge in the dry run). The locations of the five identifiable localized wave packets in EXP00 and EXP20 (i.e., WP1–WP5) are marked in (a) and (b). Please refer to Wei and Zhang (2014, 2015) for discussions of the dynamics, the potential source mechanisms, and the propagating wave characteristics of several highlighted wave packets (e.g., WP1–WP5 in EXP00 and EXP20; WP6 in EXP20 and EXP100).

vertical grid spacing on average) based on the Advanced Research version of the Weather Research and Forecasting Model (ARW; Skamarock et al. 2008), version 3.4, used in Wei and Zhang (2014; also see their section 2 for the details of the experimental design). The simulations are performed in an *f*-plane rectangular channel with 4000 km in the *x* direction, and the channel has periodic boundary conditions in the *x* direction. The nested domains are not adopted in the current study in order to avoid the possibilities of spurious reflection and distortion of waves from lateral boundaries (Park et al. 2014). There are six groups of experiments, including a dry run (EXP00), a weak moist run (EXP20), two moderate moist runs (EXP40 and EXP60), and two strong moist runs (EXP80 and EXP100). The numbers 00–100 in each experiment (EXP00–EXP100) represent the percentages of a reference relative humidity profile. Here, EXP00 and EXP100, the dry run and the full moist run, represent the experiments with zero and full initial moisture content, respectively. The initial relative humidity field in EXP100 [Fig. 1a in Wei and Zhang

(2014)] refers to the corrigendum for Tan et al. (2004). Several additional experiments (EXP80, EXP60, EXP40, and EXP20) reducing the initial relative humidity to 80%, 60%, 40%, and 20% of that in EXP100 are also performed.

The times of analysis selected for EXP00–EXP100 are listed in the caption of Fig. 1, and they are chosen based on two reasons. First, all the experiments share similar amplitudes of synoptic-scale atmospheric wind perturbations at the selected times. Figure 1 provides an overview of the large-scale baroclinic wave structures in EXP00–EXP100, as well as their corresponding moist processes (e.g., maximum convective available potential energy, 1-h precipitation accumulation, and vertically averaged positive-only latent heating rate). A description of the life cycles of dry and moist baroclinic waves can be found in section 3 of Wei and Zhang (2014). Second, the mature jet exit gravity waves have emerged in the dry run at the selected hour, not to mention those in moist experiments. Please refer to Wei and Zhang (2014, 2015) for the discussions on the

six groups of identifiable localized lower-stratospheric wave packets (e.g., WP1–WP5 in EXP00 and EXP20, whose locations are marked in Figs. 1a and 1b, and WP6 in EXP20 and EXP100, a potentially new convective gravity wave mode that is observed in moist runs long before dry jet exit wave modes become mature).

To properly evaluate the gravity wave spectral characteristics from the idealized moist baroclinic jet–front systems with varying degrees of convective instability, multidimensional discrete Fourier transforms are employed. The procedures of the calculations for all the figures in the current article are documented in the appendix, and the exact appendix sections can be found in the figure captions. Also, in this study, the mesoscale (short scale; medium scale) component represents the signal with horizontal wavelength between 50 and 600 km (between 50 and 200 km; between 200 and 600 km).

3. Gravity wave momentum flux distribution in the physical space

Gravity wave momentum flux is the most important wave characteristic that needs to be quantified to improve gravity wave drag parameterizations. Therefore, this section investigates the distribution of the density-weighted vertical flux of both zonal momentum $\rho_0 \overline{u'w'}$ and meridional momentum $\rho_0 \overline{v'w'}$, as well as their corresponding wave-driven forcing terms from the momentum equation in both the zonal direction $-(1/\rho_0)(\partial \rho_0 \overline{u'w'}/\partial z)$ and meridional direction $-(1/\rho_0)(\partial \rho_0 \overline{v'w'}/\partial z)$. The gravity wave perturbations in this section are defined as the mesoscale signal with horizontal scale between 50 and 600 km [Eq. (A10) in the appendix], which mainly follows Wang and Zhang (2007) and Lin and Zhang (2008). This definition should be sufficient to filter out synoptic waves by scale separation.

According to Eliassen and Palm's (1960) theorem, it is suggested that momentum flux would be negative if the ground-based phase velocity is slower than the mean flow for waves with positive energy flux and that deceleration of the mean flow would be expected in the presence of wave dissipation or wave breaking [also see Lindzen (1990); appendix A in Geller et al. (2013)]. Similarly, if the ground-based phase velocity is faster than the mean flow for waves with positive energy flux, momentum flux would be positive, and acceleration of the mean flow would be expected. Besides, the negative (positive) signs in $-(1/\rho_0)(\partial \rho_0 \overline{u'w'}/\partial z)$ and $-(1/\rho_0)(\partial \rho_0 \overline{v'w'}/\partial z)$ represent the momentum forcing to decelerate (accelerate) the zonal mean wind and the meridional mean wind at the corresponding level, respectively.

Figures 2 and 3 compare the horizontal view of zonal and meridional momentum flux between the six experiments at 12-km altitude. We chose the altitude of 12 km for our analysis since it is often the height of launch level of the parameterized wave source in GCMs (e.g., Geller et al. 2011) and the altitude for most field-campaign aircraft (e.g., Zhang et al. 2015).

In EXP00 (Fig. 2a), the only strong values of zonal momentum flux are the negative signals (i.e., westward momentum flux) found in the jet exit region [related to WP1 and WP2 identified in Wei and Zhang (2014)], while there is a remarkable enhancement in westward momentum flux over the WP5 region in EXP20 (compared to EXP00). For all six experiments, there is a clear dominance of westward momentum flux, while the negative centers between the ridge and the trough appear to be saturated in moderate moist runs (e.g., EXP40 and EXP60). Also, larger areas of positive values (i.e., eastward momentum flux) are found in the experiments with more initial moisture content. For meridional momentum flux (Fig. 3), negative values (i.e., southward momentum flux) dominate in EXP00, EXP20, and EXP40. However, unlike zonal momentum flux, the area for positive meridional momentum flux (i.e., northward momentum flux) can be as large as that for negative meridional momentum flux in strong moist runs (e.g., EXP80 and EXP100), and they get stronger with more initial moisture. Interestingly, in the strongest moist run (EXP100), there appears to be a separation between northward and southward momentum flux around $y = 4600$ km.

To understand the range of the momentum fluxes at the 12-km altitude and the associated forcing, Figs. 4a and 4b compare the maximum absolute values of their positive signals and negative signals. It is clearly shown in Fig. 4a that the negative fluxes are generally much stronger than the positive fluxes, except for meridional momentum flux in EXP100. Take EXP20 as an example: the maximum absolute values of the negative fluxes could be about two orders of magnitude larger than the positive fluxes. In addition, the enhancement of the negative fluxes saturates in moderate moist runs, while there is no obvious amplitude saturation in the positive fluxes. In general, the negative forcing terms are slightly stronger than the positive forcing terms (Fig. 4b), and the difference in the order of magnitude is within about 0.5. Again, a relatively weaker saturation in moderate moist runs is found in the forcing terms. In addition, Figs. 4c and 4d illustrate the maximum absolute values of positive and negative forcing terms in zonal and meridional directions at altitudes higher than 12 km. It is indicated that those forcing terms in all the experiments decrease from 12 to 17 km in altitude. For example,
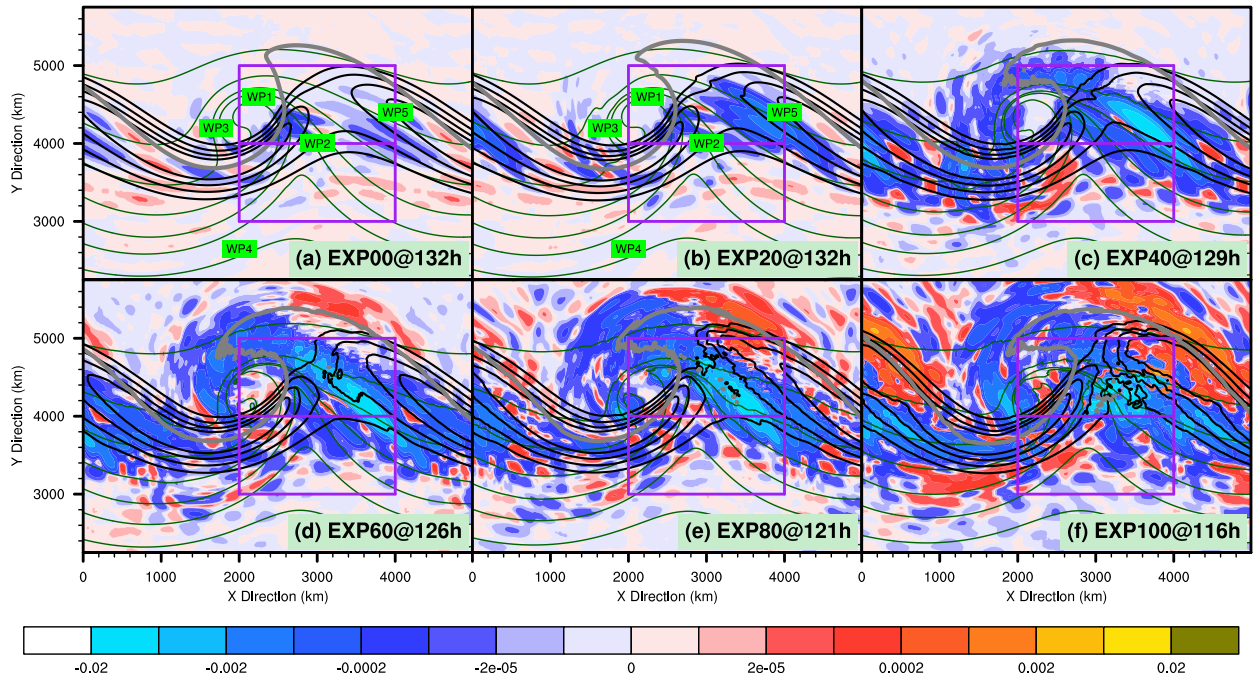
FIG. 2. The two-dimensional (x, y) space distribution of $\rho_0\overline{u'w'}$ at 12-km altitude (color fill; Pa) in EXP00–EXP100 at the selected hours listed in Fig. 1. The dark green lines, the black lines, and the marks of WP1–WP5 follow those in Fig. 1. The thick gray lines denote the potential vorticity at 7-km altitude (contours at 1.5 PVU; 1 PVU = 10^{-6} K kg^{-1} m^2 s^{-1}). The northern and southern purple boxes highlight the chosen regions for the calculations in the upper and lower panels of Fig. 15, respectively. Please refer to section c of the appendix for the details of the calculations.

EXP20 shows a sharp decline by approximately two orders of magnitude in negative forcing. Instead, there is only a relatively minor reduction in EXP100, compared to EXP00 and EXP20.

Figures 5a–c show the two-dimensional (y, z) space distribution of the zonally averaged zonal momentum flux along with potential temperature and horizontal velocity magnitude. Only three selected experiments are shown, including EXP00 (Fig. 5a), EXP20 (Fig. 5b), and EXP100 (Fig. 5c), which is also the case for Figs. 6 and 7 (as well as Fig. 10, described below). In EXP00 and EXP20, a dipole structure with the alternation of eastward and westward momentum flux is found within the jet core region (3000–5000 km in the y direction, 6–10 km in the z direction). Compared to EXP00 and EXP20, eastward momentum flux in the medium moist runs (EXP40 and EXP60) associated with the dipole is overshadowed by the intrusion of westward momentum flux. In the strong moist runs (EXP80 and EXP100), the abovementioned jet core region is completely dominated by westward momentum flux. However, the distribution of meridional momentum flux (Figs. 5d–f on EXP00, EXP20, and EXP100) is quite different from that of the zonal momentum flux. In EXP00, the lower part of the jet core region is covered by strong northward

momentum flux. In EXP20, strong southward momentum flux is found in the northern and upper part of the jet. In EXP40, the areas for the abovementioned southward momentum flux expand upward and southward, and the competition between northward and southward momentum flux continues in EXP60–EXP100. Interestingly, noticeable northward momentum flux is found in EXP60 around $y = 5000$ km from ~8-km altitude up to the model top, and those positive signals apparently become much wider toward the south and the north in EXP80 and EXP100. Generally speaking, for both zonal and meridional momentum fluxes, the signals are limited below 12 km in EXP00 (14 km in EXP20), while they can gradually reach the model top in EXP40–EXP100.

A similar pattern to Figs. 5a–c is also found in Figs. 6a–c, which demonstrates the two-dimensional (y, z) space distribution of the zonally averaged $-(1/\rho_0)(\partial\rho_0\overline{u'w'}/\partial z)$. One of the major differences is that positive zonal forcing terms are not completely overshadowed by negative zonal forcing terms even in the strong moist runs. Therefore, there is a dipole structure with both positive forcing and negative forcing in the jet core region in all experiments, which could indicate a potential change of the jet structure by gravity wave
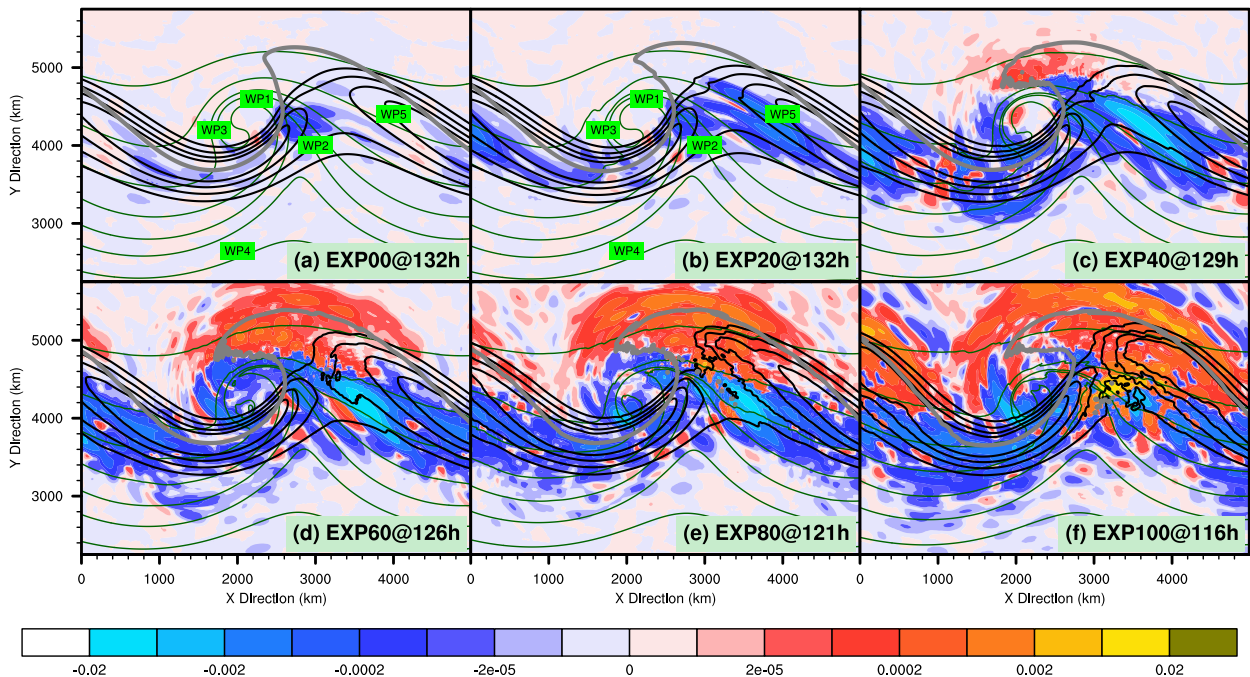
FIG. 3. As in Fig. 2, but for the two-dimensional (x, y) space distribution of $\rho_0 \overline{v'w'}$ at 12-km altitude (color fill; Pa).

dynamics. For $-(1/\rho_0)(\partial \rho_0 \overline{v'w'}/\partial z)$ (Figs. 6d–f), positive meridional forcing terms cover most of the jet core region in all experiments, especially the lower part. However, in EXP20–EXP100, the upper part of the jet core region is dominated by negative values.

Gravity wave characteristics in the current idealized simulations are also compared with those from the past observational studies. First, the typical value of the zonally averaged absolute momentum fluxes in the vicinity of the jet is approximately between 0.0005 and 0.005 Pa at 9-km altitude in all runs, as well as at 12-km altitude in moderate moist runs and strong moist runs. This resembles the observational analysis of the long-duration superpressure balloon flights from Hertzog et al. (2008) on the zonal-mean density-weighted absolute momentum fluxes from nonorographic waves, since the range of their value is approximately between 0.0005 and 0.003 Pa (thin dashed line in their Fig. 7). Nonetheless, those fluxes at 12-km altitude in the dry run and weak moist run are rather small, compared to Fig. 7 in Hertzog et al. (2008). One factor that may be at play is the relatively weak flow in the stratosphere in the current study, in contrast to the strong polar vortex over Antarctica discussed in Hertzog et al. (2007). This again emphasizes the role of moisture to obtain significant momentum fluxes, as highlighted in Plougonven et al. (2015). Furthermore, Hertzog et al. (2008) concluded in their observational studies that zonal momentum fluxes were predominantly westward and that meridional

momentum fluxes were equally northward and southward. Those results are also consistent with our findings in strong moist runs. Second, the current study indicates that the maximum amplitudes of the mesoscale horizontal wind perturbations at 9-km altitude are 3.6, 3.7, 3.9, 3.9, 3.9, and 5.5 m s^{-1} among EXP00–EXP100, respectively. Also, at 12-km altitude, those amplitudes are 0.4, 0.9, 1.9, 2.9, 3.3, and 4.8 m s^{-1} among EXP00–EXP100, respectively. This result generally fills the gap between gravity waves generated in the dry idealized baroclinic life cycles and those seen in observational case studies [e.g., horizontal wind amplitudes approximately between 5 and 10 m s^{-1}, as reported in Guest et al. (2000) and Pavelin et al. (2001)].

4. Wave spectrum in the wavenumber space

To get a better understanding of the wave properties, this section will analyze the wave spectrum in the wavenumber space based on horizontal divergence and momentum flux.

Figures 7a–c demonstrate the one-dimensional density-weighted cospectrum between the zonal velocity u and vertical velocity w along the zonal direction at 12-km altitude, which represents the two-dimensional (λ_x, y) space distribution of zonal momentum flux at that level. Here, λ_x represents the x-direction wavelength. It is shown that the baroclinic wave signals at the scale of 4000 km are almost always stronger than
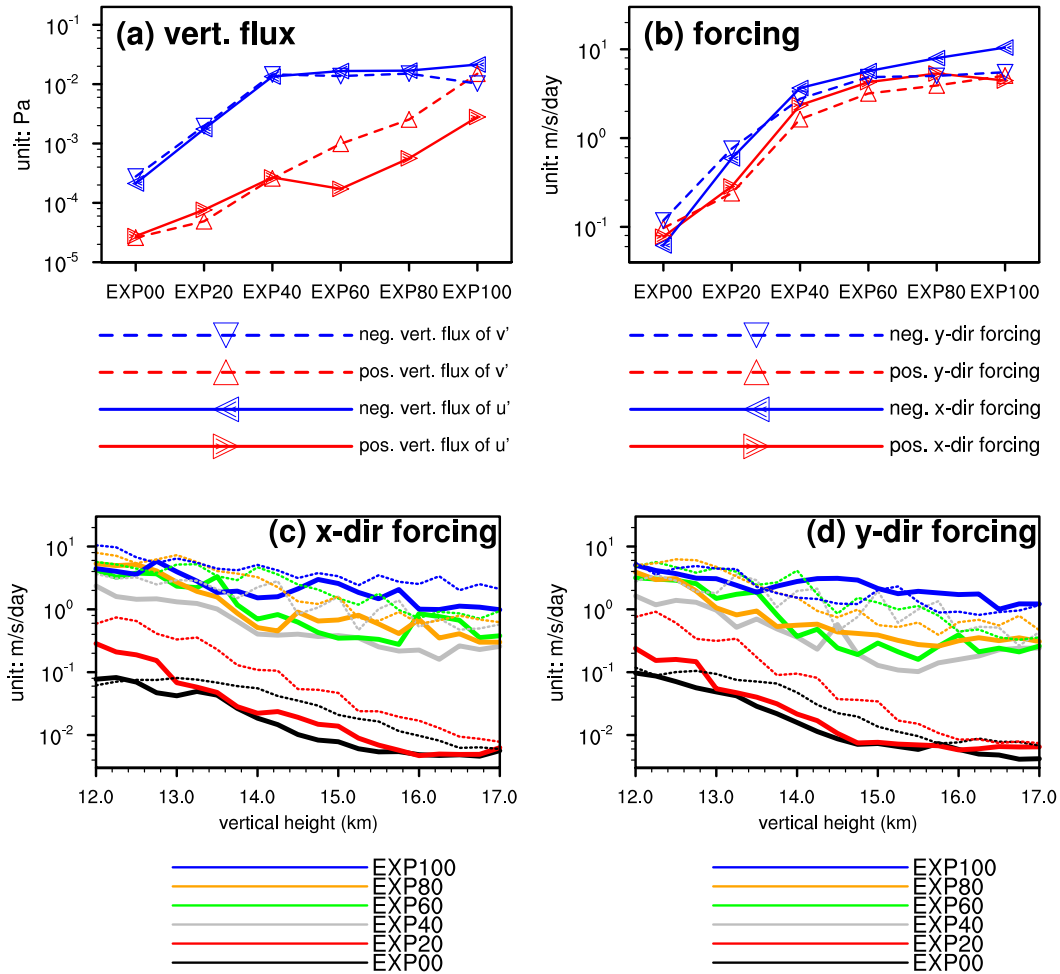
FIG. 4. The comparison of the maximum absolute values of the selected positive signals and the selected negative signals calculated over the two-dimensional horizontal model domain at (top) 12-km altitude and (bottom) at altitudes higher than 12 km in EXP00–EXP100 at the selected hours listed in Fig. 1: (a) $\rho_0\overline{u'w'}$ [positive values (red solid line); negative values (blue solid line); Pa] vs $\rho_0\overline{v'w'}$ [positive values (red dashed line); negative values (blue dashed line); Pa] at 12-km altitude; (b) $-(1/\rho_0)(\partial\rho_0\overline{u'w'}/\partial z)$ [positive values (red solid line); negative values (blue solid line); m s^{-1} day^{-1}] vs $-(1/\rho_0)(\partial\rho_0\overline{v'w'}/\partial z)$ [positive values (red dashed line); negative values (blue dashed line); m s^{-1} day^{-1}] at 12-km altitude; (c) $-(1/\rho_0)(\partial\rho_0\overline{u'w'}/\partial z)$ and (d) $-(1/\rho_0)(\partial\rho_0\overline{v'w'}/\partial z)$ at altitudes from 12 to 17 km [positive values (solid line); negative values (dashed line); m s^{-1} day^{-1}]. In (a) and (b), the x axis represents each experiment (e.g., EXP00–EXP100). In (c) and (d), the x axis represents the vertical height. In all the subplots, the y axis represents the maximum absolute values of the corresponding fluxes or forcings. Please refer to section c of the appendix for the details of the calculations.

mesoscale signals. Westward momentum flux for the scale between 320 and 640 km around $y = 4200$ km appears to be saturated or gradually getting mature in the moderate moist runs (EXP40 and EXP60), while there are much larger areas with eastward momentum flux in the strong moist runs (EXP80 and EXP100) compared to those in the dry (EXP00) and weak moist (EXP20) runs. The cospectrum analysis also reveals the sensitivity to the initial moisture content for the signals below the scale of about 80 km. For meridional momentum flux (Figs. 7d–f), the signals in EXP00–EXP40 are

dominated by northward momentum flux north of around $y = 4600$ km. However, in the strong moist runs, there is a slight preference of positive values north of $y = 4000$ km, which suggests that northward momentum flux tends to expand southward with the increasing initial moisture content.

Figure 8 depicts the two-dimensional wavenumber-space (k^*, l^*) distribution of the power spectral density based on the horizontal divergence at 12-km altitude among six experiments. Here, the zonal k^* and meridional l^* wavenumbers, indicate how many waves of
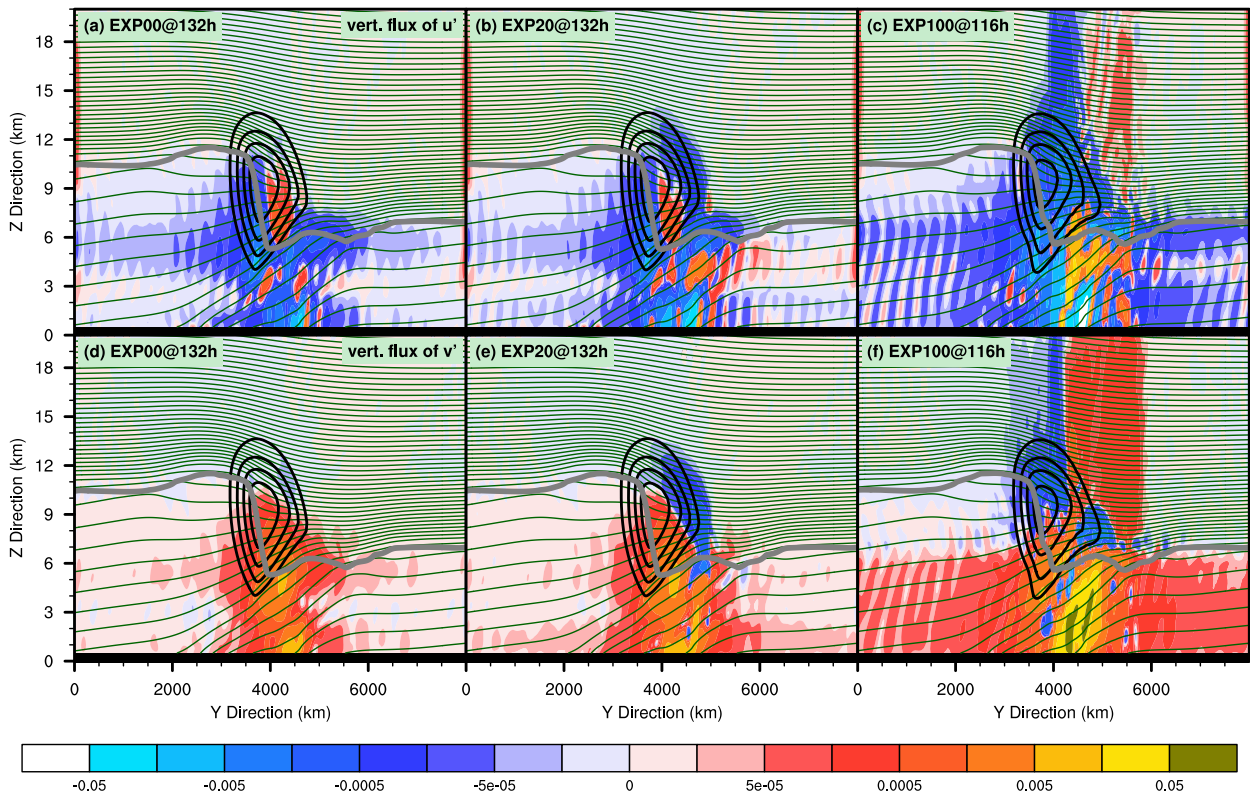
FIG. 5. The two-dimensional (y, z) space distribution of the zonally averaged (top) $\rho_0 \overline{u'w'}$ and (bottom) $\rho_0 \overline{v'w'}$ (color fill; Pa), the potential temperature (dark green lines; contours at every 5 K), and the horizontal velocity magnitude (black lines; contours from 30 to 65 m s^{-1} at every 5 m s^{-1}) in (a),(d) EXP00; (b),(e) EXP20; and (c),(f) EXP100 at the selected hours listed in Fig. 1. The thick gray lines denote the location of the tropopause where potential vorticity equals 1.5 PVU. Please refer to section c of the appendix for the details of the calculations.

x-direction wavelength λ_x and y-direction wavelength λ_y fit the length of the selected domain in the x and y directions, respectively. It is shown that the mesoscale power spectra in moist runs are much greater than those in the dry run. In all the experiments, the power appears to be highly anisotropic. For the short scales (Figs. 8a–f), the weak moist run of EXP20 has a remarkable enhancement in power along approximately 45° (the polar coordinate is used to identify the angle in this paper), relative to the dry run of EXP00. Note that this direction also corresponds to the primary axis of the jet. Furthermore, the distribution of spectral power in strong convective cases (EXP80 and EXP100) appears to be more homogeneous along all angles (relative to EXP00 and EXP20), even though the power along approximately 45° is still somewhat stronger. This is again evidence for the existence of convective gravity waves, in addition to jet–front gravity waves, for the strong moist cases. For the medium scales (Fig. 8g–l), EXP20 continues to have stronger power along approximately 45° (relative to EXP00). Interestingly, it is worth mentioning that the power maxima along approximately 45°

appear to migrate upscale from EXP40 to EXP100. For example, the peak in EXP40 locates around the scale of 200 km, while the peak in EXP100 is found within scales between 400 and 600 km.

In addition to Fig. 8, Fig. 9 compares its corresponding one-dimensional λ_H space distribution (λ_H indicates global horizontal wavelength). For the power spectra based on the entire (k^*, l^*) wavenumber space (Fig. 9a), there is an almost two orders of magnitude difference between EXP00 and EXP20 for the short scales, while noticeable enhancement can also be found for the medium scales. Generally speaking, the power is stronger with more initial moisture content, even though EXP40–EXP100 share comparable power around the scale of 200 km. Figure 9b compares the power spectra between the space for $k^*l^* > 0$ and that for $k^*l^* < 0$. Interestingly, in all experiments, the mesoscale power spectra for $k^*l^* > 0$ are generally greater than those for $k^*l^* < 0$. Nonetheless, they are relatively comparable for the short scales in EXP80 and EXP100, which further suggests that the distribution of power in strong convective cases may be more
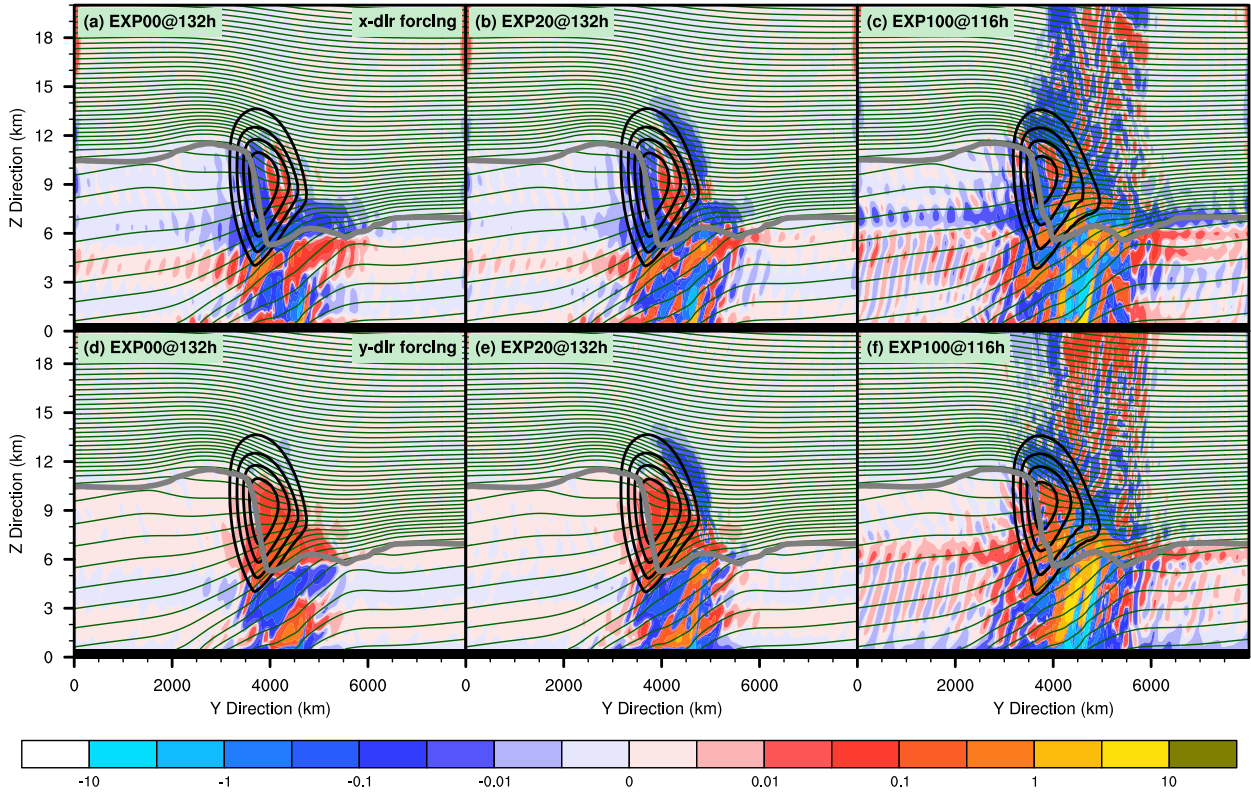
FIG. 6. As in Fig. 5, but for the two-dimensional (y, z) space distribution of the zonally averaged (a)–(c) $-(1/\rho_0)(\partial\rho_0\overline{u'w'}/\partial z)$ and (d)–(f) $-(1/\rho_0)(\partial\rho_0\overline{v'w'}/\partial z)$ (color fill; m s^{-1} day^{-1}).

homogeneous along all angles than that in the dry or weak moist run.

Following Fig. 8, the distribution of zonal momentum flux in the two-dimensional (k^*, l^*) wavenumber space is shown in the upper panels of Fig. 10. For the short scales (Figs. 10a–c), there is no obvious strong signal in EXP00, while westward momentum flux emerges in EXP20 along approximately 45°. In EXP40, there are larger areas of westward momentum flux in the entire (k^*, l^*) space for both $k^*l^* > 0$ and $k^*l^* < 0$. With an increasing initial moisture content, more areas of eastward momentum flux are found, even though westward momentum flux continues to dominate the (k^*, l^*) space for $k^*l^* < 0$. Interestingly, in the (k^*, l^*) space for $k^*l^* > 0$ in EXP100, both eastward and westward momentum fluxes are important. For the medium scales (Figs. 10g–i), westward momentum flux in EXP20 is enhanced with a larger area compared to EXP00, while the centers of westward momentum flux in the (k^*, l^*) space for $k^*l^* > 0$ appear to be slightly deepened with a higher initial moisture content.

In addition to the upper panels of Fig. 10, the distribution of meridional momentum flux in two-dimensional (k^*, l^*) space is also investigated (the lower panels of Fig. 10). For the short scales (Figs. 10d–f), the areas of strong southward momentum flux in the (k^*, l^*) space for $k^*l^* > 0$ apparently get larger from EXP00 to EXP40, while those for strong northward momentum flux are almost negligible. However, from EXP60 to EXP100, northward momentum flux gradually becomes as important as (or even more important than) southward momentum flux in the (k^*, l^*) space for $k^*l^* > 0$. Instead, in the (k^*, l^*) space for $k^*l^* < 0$, northward momentum flux appears to dominate, especially from EXP60 to EXP100. For the medium scales (Figs. 10j–l), most of the strong southward momentum flux is found in the (k^*, l^*) space for $k^*l^* > 0$ (along approximately 45° from EXP20 to EXP100), while most of the strong northward momentum flux is found in the (k^*, l^*) space for $k^*l^* < 0$.

5. Momentum fluxes as a function of phase velocity

The relationship between vertical flux of horizontal momentum and ground-based phase velocity is directly relevant to the wave source spectrum that needs to be specified in gravity wave drag parameterizations (e.g., Lindzen 1981; Alexander and Dunkerton 1999). It is
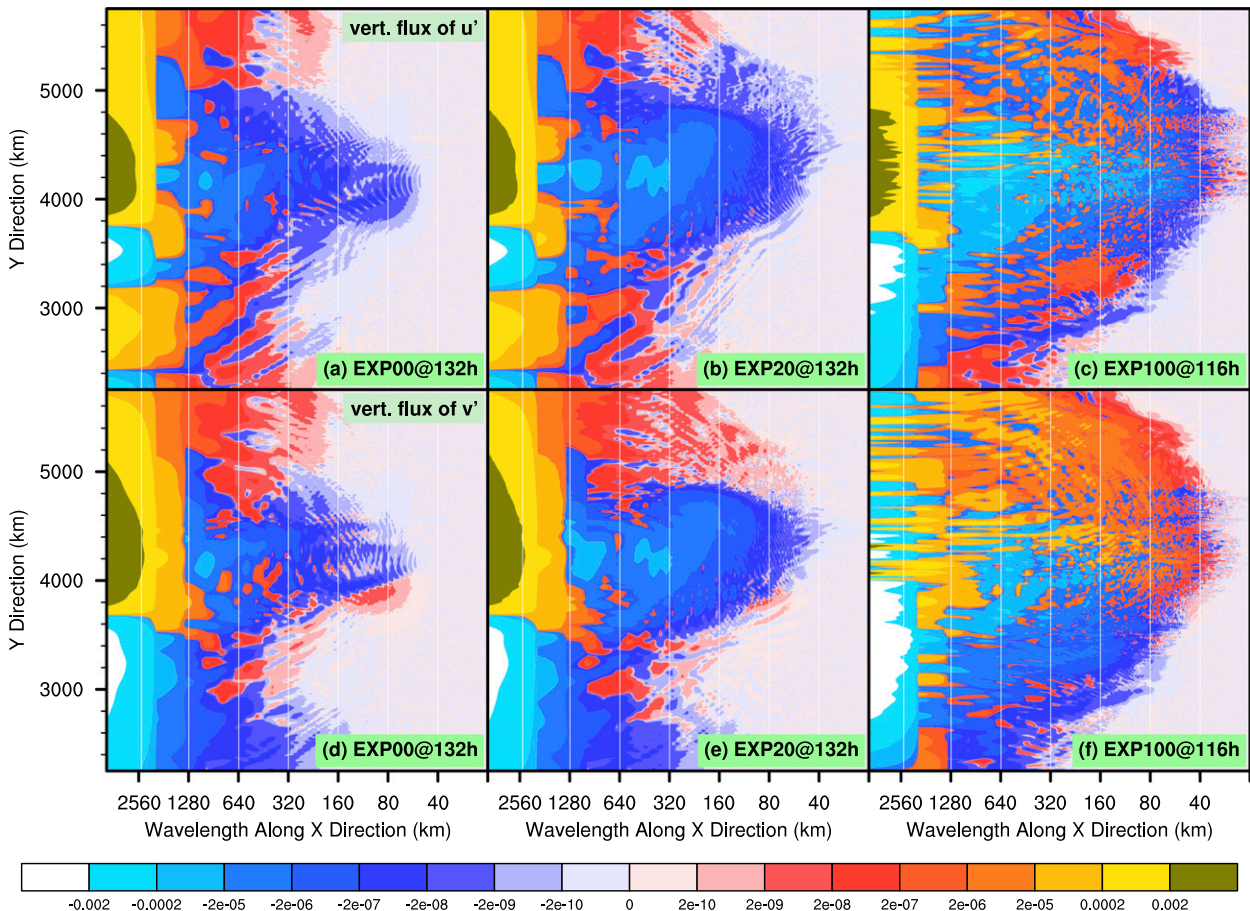
FIG. 7. The two-dimensional (λ_x, y) space distribution of (a)–(c) $\rho_0 \overline{u'w'}$ and (d)–(f) $\rho_0 \overline{v'w'}$ at 12-km altitude (color fill; Pa wavenumber^{-1}) based on the one-dimensional density-weighted cospectrum between the corresponding horizontal velocity component and vertical velocity component at each y. The horizontal axis represents wavelength along the x direction λ_x, and the vertical axis represents the y direction in the model domain. Three experiments are shown [EXP00 in (a) and (d); EXP20 in (b) and (e); and EXP100 in (c) and (f)], and their selected hours follow Fig. 1. Please refer to section d of the appendix for the details of the calculations.

largely the distribution of momentum flux across wave phase speeds that determines where gravity waves break and how much wave forcing they apply to the mean flow. This section presents the distribution of momentum fluxes in phase velocity space, for direct relevance to gravity wave parameterizations. This complements Kim et al. (2016), especially with respect to their Fig. 9 on the momentum flux phase speed spectra at 8-km altitude in their dry idealized simulations.

Figure 11 demonstrates the two-dimensional (c_{px}, y) space distribution of zonal momentum flux at 12-km altitude for all experiments within 48 h, while the corresponding comparison of the one-dimensional c_{px} space distribution at six selected y positions is shown in Fig. 12. Here, c_{px} represents the ground-based gravity wave phase velocity along the x direction. It is found in all experiments that the peak in westward momentum flux locates around the estimated ground-based baroclinic

wave phase velocity along the x direction of $13.9 \, \text{m s}^{-1}$, illustrated by the dark green lines in Fig. 11. O'Sullivan and Dunkerton (1995) and Plougonven and Snyder (2007) have already pointed out that gravity wave packets are nearly stationary with respect to the synoptic-scale baroclinic wave along the zonal direction, even though their experiments are based on a dry atmosphere only. Furthermore, as the initial moisture content increases, a dipole structure pattern with westward momentum flux at slower speeds and eastward momentum flux at faster speeds is becoming clearer, and the spectrum for both fluxes is getting wider in phase speeds. In addition, the centers for westward momentum flux are generally stronger than those for eastward momentum flux at all the selected y positions in Fig. 12. It is also interesting to point out that the boundary between eastward and westward momentum fluxes broadly matches the zonally averaged zonal velocity
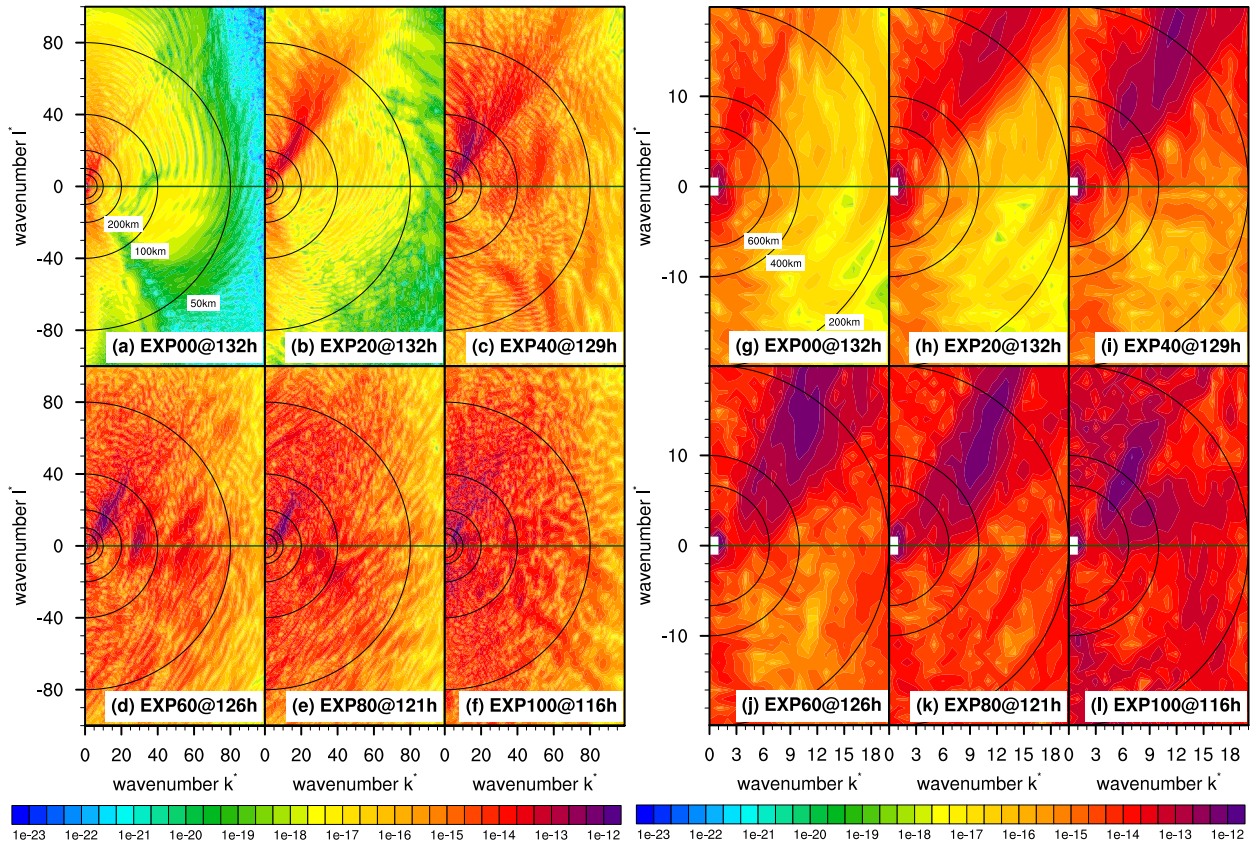
FIG. 8. The two-dimensional (k^*, l^*) space distribution of the power spectral density based on the two-dimensional discrete Fourier transform of the horizontal divergence at 12-km altitude (color fill; s^{-2} wavenumber^{-1} wavenumber^{-1}) in (a),(g) EXP00 at 132 h; (b),(h) EXP20 at 132 h; (c),(i) EXP40 at 129 h; (d),(j) EXP60 at 126 h; (e),(k) EXP80 at 121 h; and (f),(l) EXP100 at 116 h. The horizontal (vertical) axis represents wavenumber k^* (l^*), which indicates how many waves fit the length of the selected domain in the x (y) direction (i.e., 4000 km in both the x and y direction). The negative part of the x direction is not shown because of the symmetry about the point (0, 0). The black curves show the global horizontal wavelength at 50 km [marked in (a)], 100 km [marked in (a)], 200 km [marked in (a) and (g)], 400 km [marked in (g)], and 600 km [marked in (g)]. The dark green horizontal lines show zero wavenumber l^*. The scale above 50 km is demonstrated in (a)–(f) mainly to highlight the short-scale waves (scale within 50–200 km), while in (g)–(l) the scale is zoomed in above 200 km to highlight the medium-scale waves (scale within 200–600 km). Please refer to section a of the appendix for the details of the calculations.

component (black curves in Fig. 11), which appears to be consistent with the theoretical description of Eliassen and Palm (1960) on the relationship between the mean flow and the phase velocity.

Figure 13 continues to reveal the mesoscale component of zonal momentum flux in the space of ground-based horizontal gravity wave phase velocity. One feature that all the experiments have in common is the westward momentum flux along approximately 45° at the speed between 10 and 20 m s^{-1}, even though the exact strength/shape of the negative signals could be modified by the moist process. In EXP00 and EXP20, noticeable westward momentum fluxes can only be found within the first quadrant (especially along approximately 45°). In comparison, there are noticeable westward momentum fluxes within all four quadrants

along almost all possible angles in EXP40 and EXP60, while those fluxes continue to expand toward faster speeds in EXP80 and EXP100. Similarly, relatively strong eastward momentum fluxes also expand toward faster speeds, as the initial moisture content increases. However, eastward momentum fluxes differ from westward momentum fluxes in at least two major aspects. First, along all possible angles in the horizontal phase velocity space, strong eastward momentum fluxes generally locate in faster velocity than strong westward momentum fluxes. Second, most of the strong eastward momentum fluxes only locate in the first and fourth quadrants. Note that both of the abovementioned differences could be explained by the Eliassen and Palm (1960) theorem (assuming the background zonal velocity is generally positive). With that being said, for
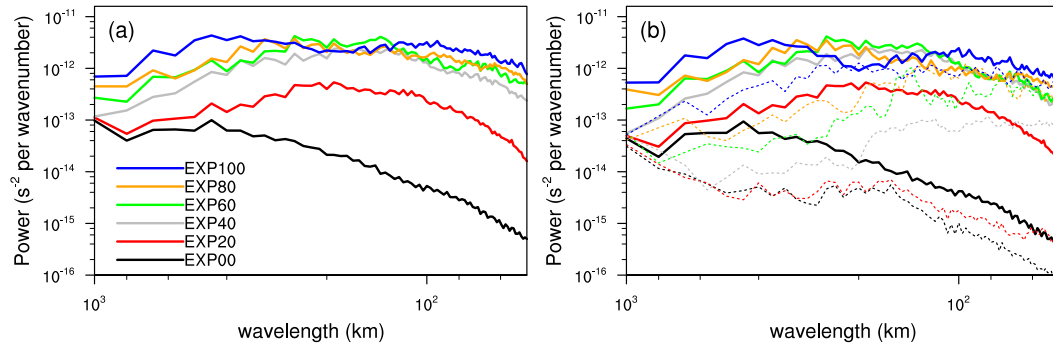
FIG. 9. The one-dimensional λ_H space distribution of power spectra of the horizontal divergence at 12-km altitude in EXP00–EXP100 at the selected hours listed in Fig. 1. The horizontal axis represents the global horizontal wavelength λ_H (km), and the vertical axis represents its corresponding power (s^{-2} wavenumber^{-1}). (a) The power spectra based on the entire (k^*, l^*) space (solid lines); (b) a comparison of the power spectra based on part of the (k^*, l^*) space between $k^*l^* > 0$ [i.e., the first and third quadrants in (k^*, l^*) space (solid lines)] and $k^*l^* < 0$ [i.e., the second and fourth quadrants in (k^*, l^*) space (dashed lines)]. Please refer to section b of the appendix for the details of the calculations.

upward-propagating gravity waves, it may be hard to explain positive momentum fluxes with phase speeds smaller than background wind based on the Eliassen and Palm (1960) theorem. For the 48-h period over a large

horizontal domain, there could be a wide range of possibilities for the background flows (e.g., changes in the zonal-mean zonal wind), wave characteristics, and sources. Also, when both negative and positive
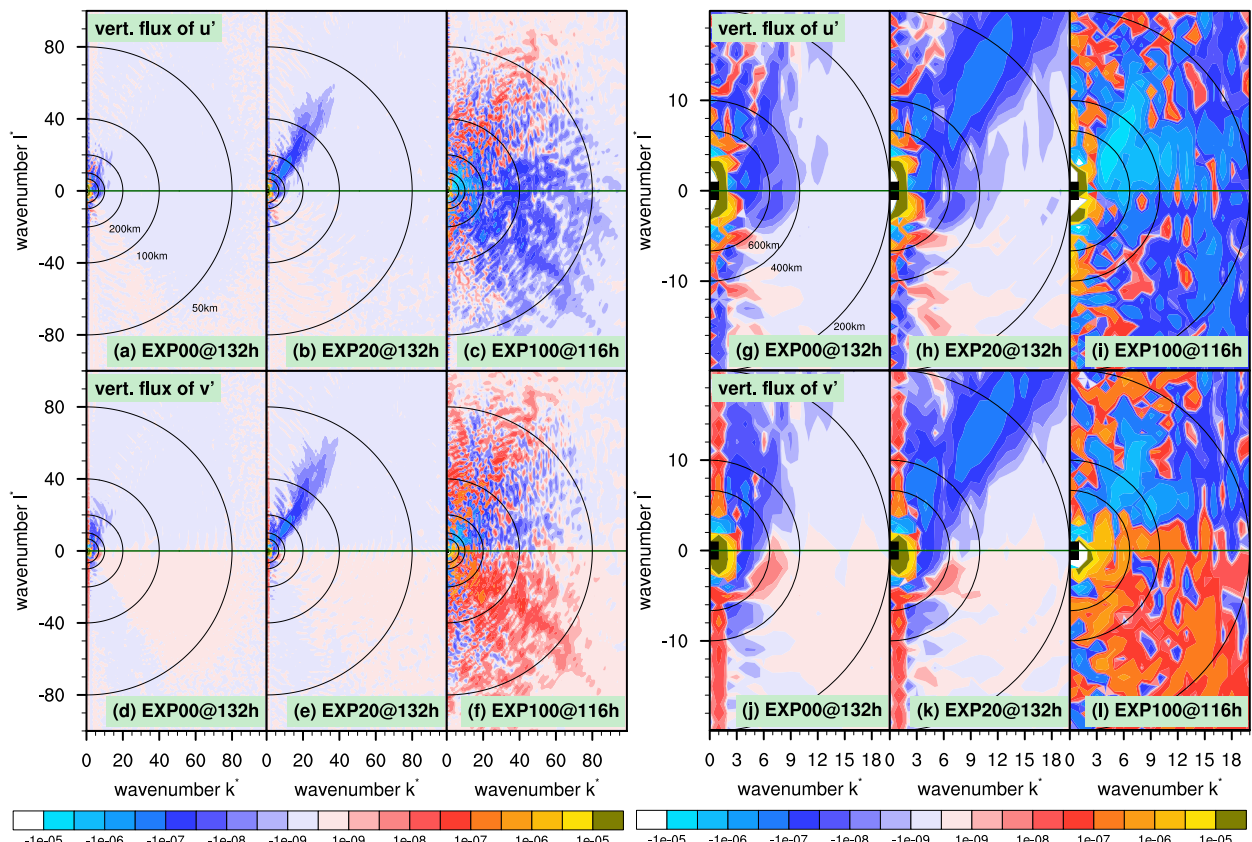

FIG. 10. As in Fig. 8, but for the two-dimensional (k^*, l^*) space distribution of (a)–(c),(g)–(i) $\rho_0\overline{u'w'}$ and (d)–(f),(j)–(l) $\rho_0\overline{v'w'}$ based on the density-weighted cospectrum between the two-dimensional discrete Fourier transform of the corresponding horizontal velocity component and that of the vertical velocity component at 12-km altitude (color fill; Pa wavenumber^{-1} wavenumber^{-1}). Three experiments are shown [EXP00 in (a),(d),(g),(j); EXP20 in (b),(e),(h),(k); and EXP100 in (c),(f),(i),(l)], and their selected hours follow Fig. 1.

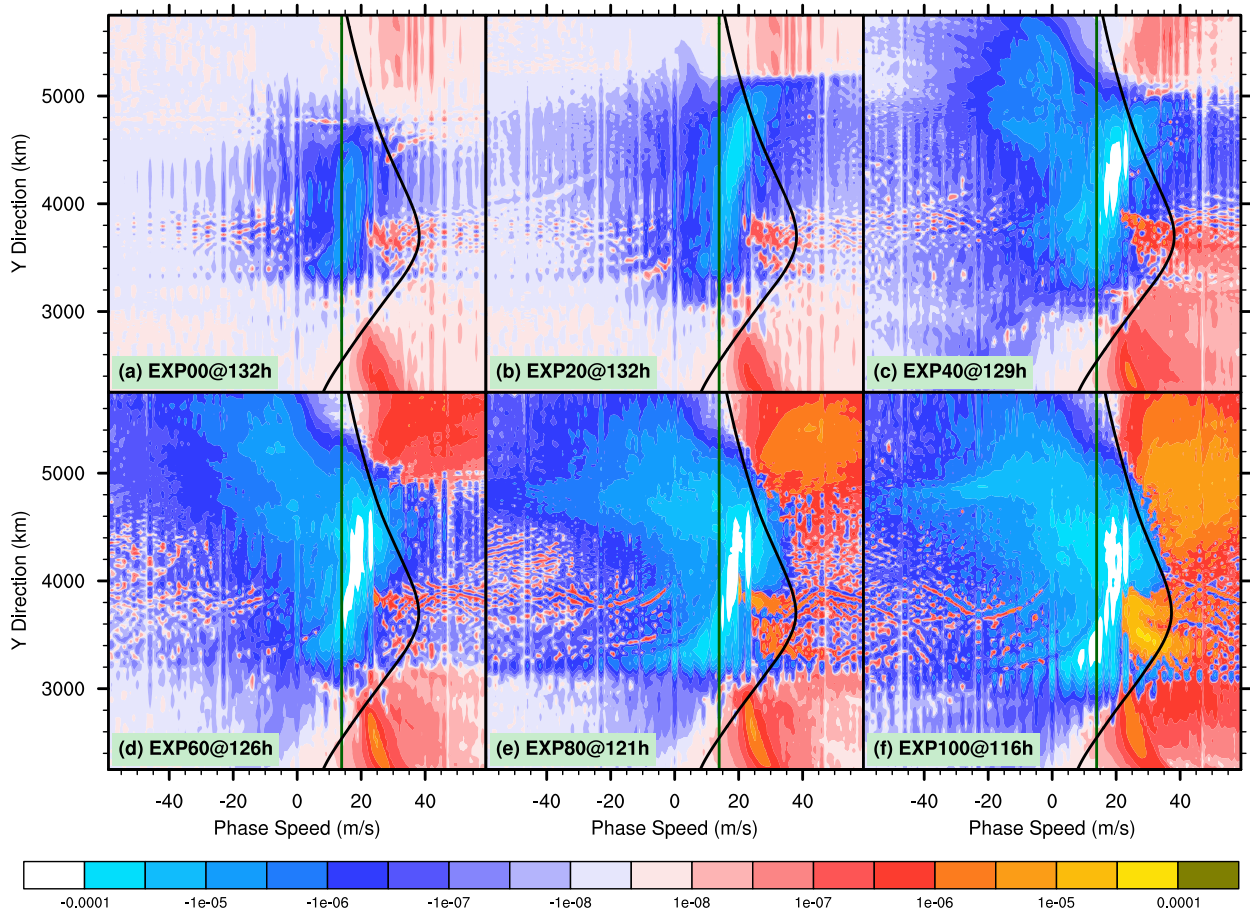FIG. 11. The two-dimensional (c_{px}, y) space distribution of $\rho_0 \overline{u'w'}$ at 12-km altitude [color fill; Pa $(\mathrm{m\,s^{-1}})^{-1}$] based on the density-weighted cospectrum between the two-dimensional discrete Fourier transform of zonal velocity component and that of vertical velocity component within 48 h at each y. The horizontal axis represents the ground-based gravity wave phase velocity along the x direction c_{px}, and the vertical axis represents the y direction in the model domain. The resolution of c_{px} is $1\,\mathrm{m\,s^{-1}}$. The vertical dark green lines denote the estimated ground-based baroclinic wave phase velocity along the x direction (i.e., $13.9\,\mathrm{m\,s^{-1}}$). The black curves denote the zonally averaged zonal velocity component. The shown experiments and the selected hours follow Fig. 1. Please refer to section e of the appendix for the details of the calculations.

momentum fluxes exist for phase speeds smaller than the background wind, there might be downward-propagating gravity waves or in situ gravity waves at around 12-km altitude.

Following Fig. 13, the corresponding short-scale components and medium-scale components among three selected experiments (i.e., EXP20, EXP60, and EXP100) are plotted in Fig. 14. At least three properties could be used to distinguish the abovementioned two components. First, under the influence of the moist process, the short-scale component gradually has a wider distribution in the horizontal phase velocity space, relative to the medium-scale component. Particularly, it shows a stronger tendency for both eastward and westward momentum fluxes to expand toward faster phase speeds with increasing moisture. In comparison, the

medium-scale component also contributes a large portion of the westward momentum fluxes, but within a limited horizontal phase velocity space. Second, under the influence of the moist process, the short-scale component gradually has a more symmetric distribution about the horizontal green line (i.e., the axis for the zero values in the meridional component of horizontal phase velocity), while the asymmetry for the medium-scale component can be indicated by the outstanding westward momentum flux in the first quadrant. Third, the resemblance between six experiments for the medium-scale component is remarkable, especially within the first quadrant from EXP40 to EXP80. Therefore, this comparison in Fig. 14 suggests that the distribution for the short-scale component in the horizontal phase velocity space is more sensitive to the increasing initial
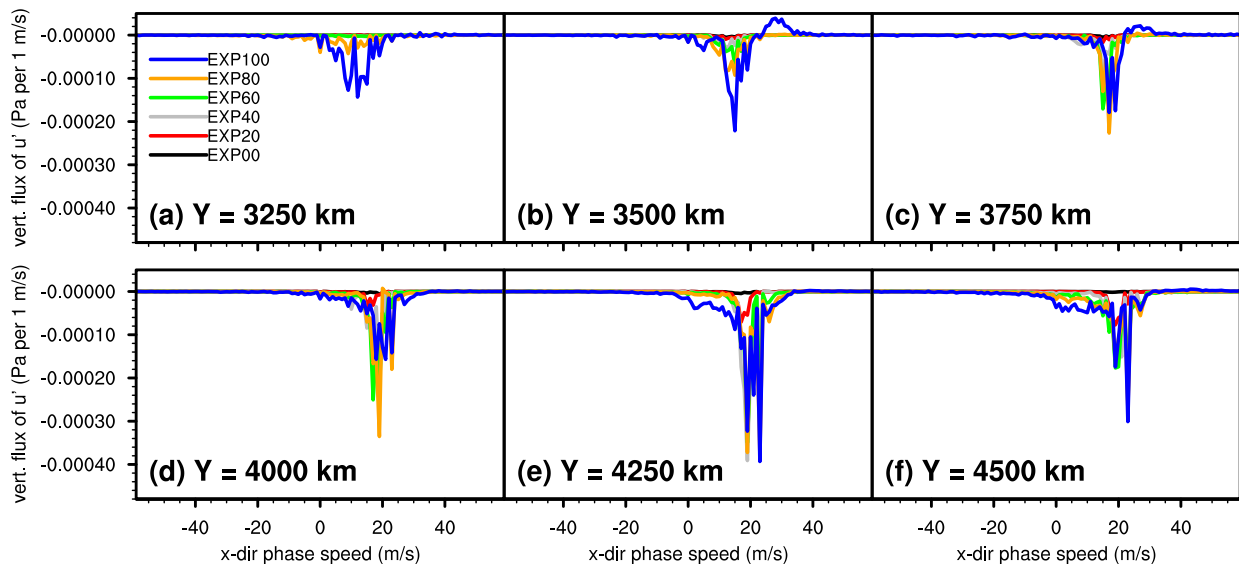
FIG. 12. The comparison of the one-dimensional c_{px} space distribution of $\rho_0\overline{u'w'}$ at 12-km altitude [Pa (m s^{-1})$^{-1}$] among EXP00–EXP100 at each selected y: (a) 3250, (b) 3500, (c) 3750, (d) 4000, (e) 4250, and (f) 4500 km. The horizontal axis (including its resolution) and the calculation of $\rho_0\overline{u'w'}$ follow Fig. 11.

moisture content (and thus the degree of moist instability), compared with the medium-scale component.

To investigate the sensitivity of the momentum flux phase speed spectra to the locations, the calculation in Fig. 13 is used again but within multiple selected local regions instead of the entire horizontal model domain of interest. The analysis demonstrates that each individual region has its own uniqueness and characteristics and that their combination would be broadly consistent with Fig. 13. For simplicity, only two examples (Figs. 15a–c vs Figs. 15d–f) are highlighted in this paper to compare the horizontal phase velocity space distribution of zonal momentum flux within two neighboring local regions (i.e., the northern purple box in Fig. 2 vs the southern purple box in Fig. 2 or the local region that covers the jet exit region above the surface occluded front vs the local region that locates to the south of the jet exit region). In Fig. 15, only three selected experiments are shown to avoid redundancy, and they are EXP20, EXP60, and EXP100. First, most of the strong westward momentum fluxes lie in the first quadrant in all six experiments from the spectra based on the southern local region, while the northern local region has those fluxes in the first quadrant in EXP00–EXP20 and all of the four quadrants in EXP40–EXP100. Second, under the influence of moist processes, most of the strong eastward momentum fluxes can be identified in the fourth quadrant from the spectra based on the southern local region, while the northern local region has those fluxes in the first quadrant. Third, under the influence of moist processes,

compared to the northern local region, the southern local region manifests narrower spectra with a less efficient expansion toward fast phase velocity along almost all directions, except for the angles approximately between 270° and 315°. For example, in EXP100, the northern region has relatively strong westward momentum fluxes even at velocities higher than 20 m s^{-1} for the angles approximately between 90° and 270°, while the southern region only shows very weak fluxes at slow velocities over the abovementioned angles.

6. Concluding remarks and discussion

Based on the high-resolution mesoscale models of the idealized moist baroclinic jet–front system used in Wei and Zhang (2014), this study investigates the gravity wave spectral characteristics in order to understand how to improve nonorographic gravity wave parameterization in general circulation models. In total, there are six experiments with varying degrees of convective instability. We find that, at the altitude of 12 km, negative zonal momentum flux (i.e., westward momentum flux) dominates; however, negative as well as positive values of momentum flux (i.e., eastward momentum flux) are noted in the experiments with increasing initial moisture content and thus stronger moist instability. In addition, the negative values (i.e., southward momentum flux) dominate the meridional momentum vertical flux in the dry and weak moist runs and one of the moderate moist runs, while positive momentum fluxes (i.e., northward
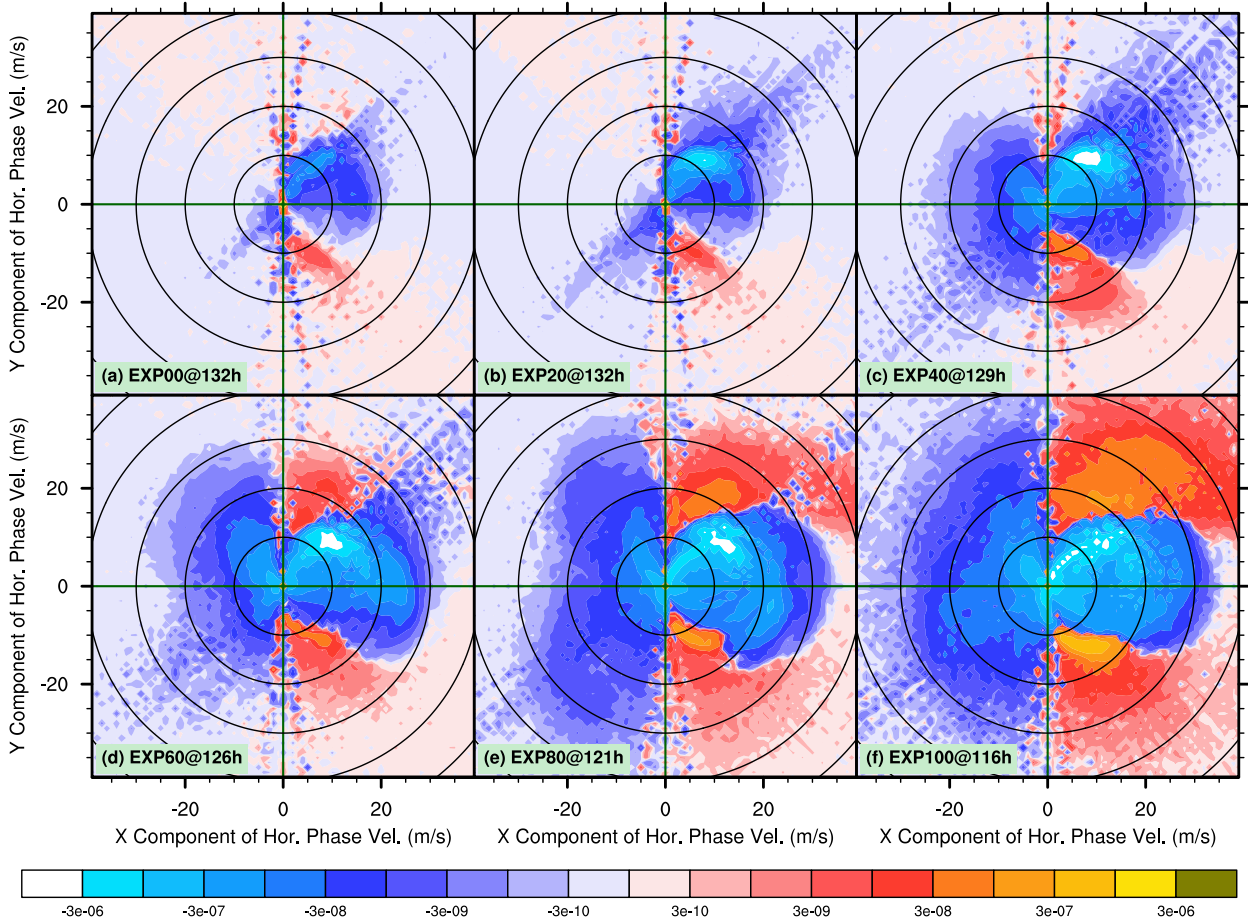
FIG. 13. The two-dimensional (C_{HP_x}, C_{HP_y}) space distribution of $\rho_0 \overline{u'w'}$ at 12-km altitude [color fill; Pa (m s^{-1})$^{-2}$] based on the density-weighted cospectrum between the three-dimensional discrete Fourier transform of the zonal velocity component and that of the vertical velocity component within 48 h. The x (y) axis represents the x (y) component of the ground-based horizontal gravity wave phase velocity (C_{HP_x}, C_{HP_y}). The resolution of C_{HP_x} (C_{HP_y}) is 1 m s^{-1}. The black curves show the magnitude of (C_{HP_x}, C_{HP_y}) at each 10 m s^{-1}. The horizontal (vertical) dark green lines show zero C_{HP_y} (C_{HP_x}). The shown experiments and the selected hours follow Fig. 1. Please refer to section f of the appendix for the details of the calculations.

momentum flux) are as large as the negative ones in strong moist runs.

This study also investigates the vertical gradient of momentum flux in order to understand its forcing in the momentum equation. Future work will attempt to estimate other wave-induced flux terms and the corresponding forcing in momentum or entropy (Miyahara 2006; Achatz et al. 2010), which could be potentially important and should probably be parameterized (Shutts and Vosper 2011).

Our study clearly shows that, in all of our simulations, the peak in westward momentum flux is near the baroclinic wave phase speed along the zonal direction (i.e., ~13.9 m s^{-1} by model design). As initial moisture content of the baroclinic system increases, both westward and eastward momentum fluxes increase. However, even in the full moisture case, eastward

momentum flux is much smaller than westward momentum flux.

Our experiments show the different behaviors of gravity wave spectral characteristics between gravity waves with short and medium horizontal scales. For the short scales between 50 and 200 km, wave momentum flux along the direction of the jet is enhanced remarkably in the weak moist run (relative to the dry run), while the strong moist cases have a relatively better isotropy in the two-dimensional wavenumber space distribution of horizontal divergence or a relatively better line symmetry about the zero meridional component of horizontal phase velocity in zonal momentum flux versus phase speed (relative to the dry run and the weak moist run). For the medium scales between 200 and 600 km, the weak moist run continues to have stronger power along the direction of the jet, while the
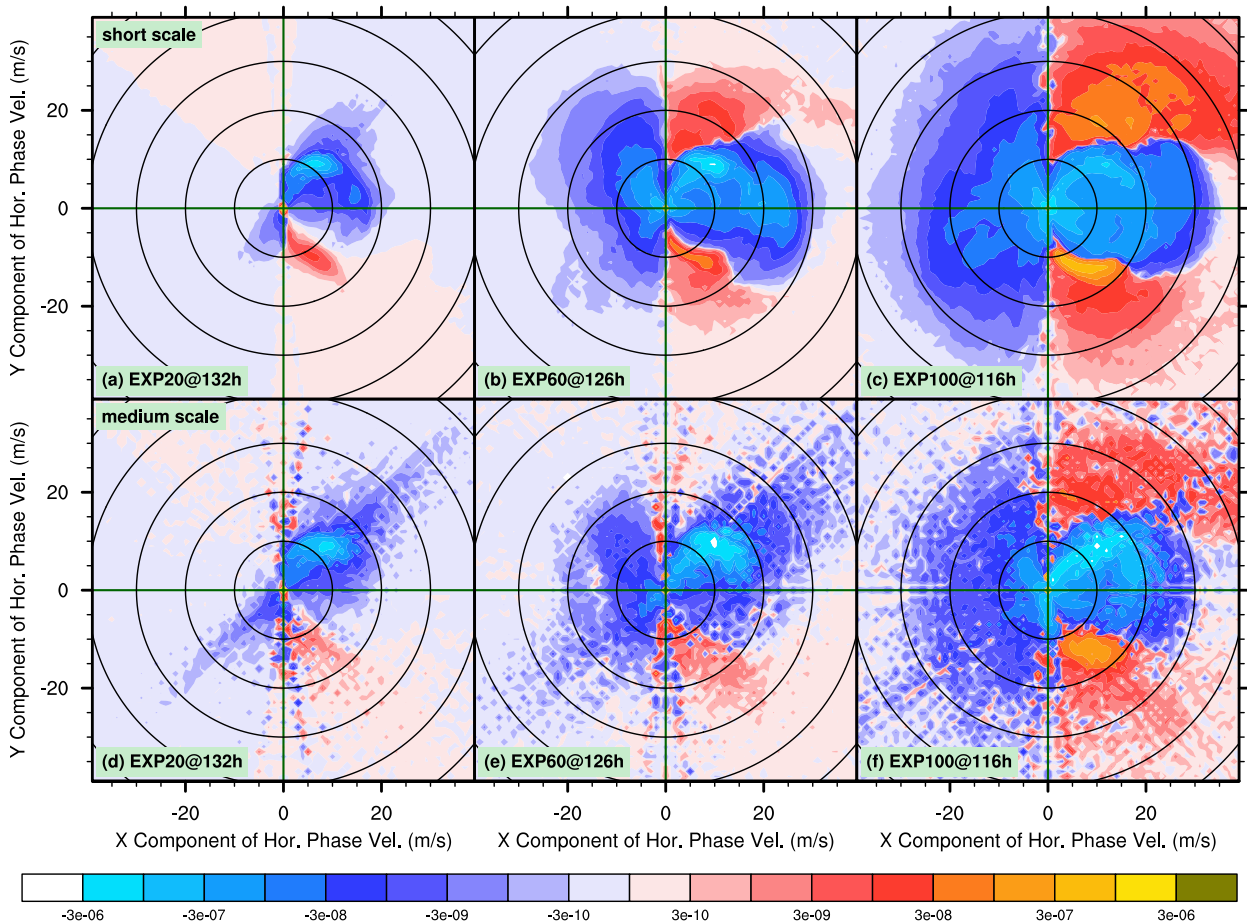
FIG. 14. As in Fig. 13, but calculated for (a)–(c) the short-scale waves with horizontal scale between 50 and 200 km and (d)–(f) the medium-scale waves with horizontal scale between 200 and 600 km. Three experiments are shown [EXP20 in (a) and (d); EXP60 in (b) and (e); and EXP100 in (c) and (f)], and their selected hours follow Fig. 1.

strong moist cases are still highly anisotropic or asymmetric (compared to the behaviors in the short scales). Furthermore, the comparison in zonal momentum flux versus phase speed suggests that the short-scale component is more sensitive to the increasing initial moisture content, likely because of stronger convectively generated gravity waves, in addition to the jet-related gravity waves.

Our study suggests that the spectral characteristics of gravity waves generated in the moist baroclinic jet–front systems differ among the potential source mechanisms: upper-level jet versus surface front versus moist convection. For example, as the initial moisture content increases, one could identify 1) more positive fluxes, 2) a wider and stronger spectrum toward faster phase velocity or higher wavenumber, 3) stronger fluxes or forcing terms at much higher altitudes, and 4) a relatively quasi-symmetric distribution in short-scale component. Therefore, we confirm that the dry gravity wave

source (i.e., upper jet and/or surface front in the current study) has a relatively narrower and less symmetrical spectrum dominated by negative momentum flux, centered around a low phase velocity, and that the moist gravity wave source (i.e., moist convection) contributes to the generation of a spectrum that is broader in phase speed and more symmetrical. Such wave characteristics are consistent with the theoretical derivations of gravity wave characteristics by a three-dimensional heating source (Beres 2004; Song and Chun 2005). Furthermore, as hypothesized in Wei and Zhang (2014), 1) in a dry experiment, dry dynamic gravity wave modes are believed to be generated through spontaneous balance adjustment hypothesis (Zhang 2004); 2) in a weak moist experiment, dry dynamic gravity wave modes continue to dominate, while being noticeably enhanced or partially modified by convective mode or moist process; and 3) in a strong moist experiment, the convective mode or moist process is soon fully coupled with other modes and
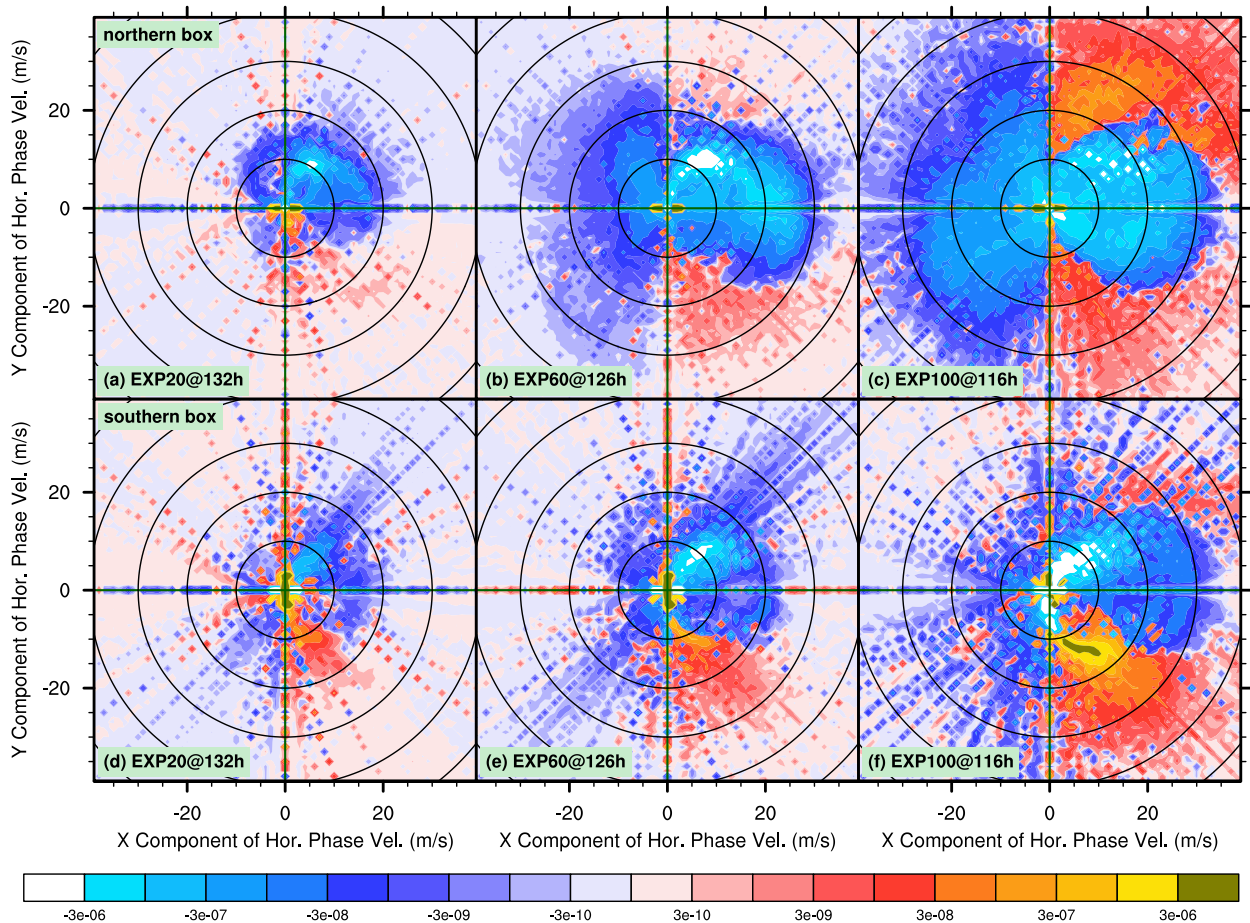
FIG. 15. As in Fig. 13, but calculated within (a)–(c) the northern purple box and (d)–(f) the southern purple box in Fig. 2. Three experiments are shown [EXP20 in (a) and (d); EXP60 in (b) and (e); and EXP100 in (c) and (f)], and their selected hours follow Fig. 1.

background flow as baroclinicity increases over time. Therefore, to improve nonorographic gravity wave parameterizations, it is important to include the effects of dry wave modes generated by jets and fronts, which could be modified or enhanced by the moist processes. In the cases with strongly moist instability, it might be necessary to combine both parameterization schemes for convective and jet–front gravity waves.

Last, this work suggests that the treatment for the nonorographic gravity wave parameterization should depend on their locations relative to the moving sources. In particular, a strong meridional dependence of gravity wave spectral characteristics can be verified, in addition to a potentially strong altitude variation.

Other important issues, such as the sensitivity to model resolution and the choice of convective parameterizations, have been discussed or justified by previous studies. Wei and Zhang (2014, their section 6c) showed that the excited waves in the idealized simulations with 5-km horizontal grid spacing are similar to those in the

simulations with 10-km grid spacing, especially for the medium-scale waves. Regarding convective parameterizations, Stephan and Alexander (2014) have shown that the simulated gravity wave spectrum was fairly insensitive to the physics parameterization choices. Future research will continue to evaluate the spatial and temporal variations in the gravity wave characteristics. Those upcoming analyses, along with the current study and some of the previous studies, will help to guide the jet–front gravity wave parameterization under various moist conditions, including the derivation for the phase speed spectrum of source-level gravity wave momentum flux, as well as the magnitude of the momentum flux.

APPENDIX

Space Transformation Based on Discrete Fourier Transforms

In the current study, the baroclinic wave simulations have a four-dimensional (x, y, z, t) space. For example, the zonal velocity component u is a function of x, y, z, and t. Because of the complexity of the data, it is necessary to reduce or transform the dimensions for different purposes. In this appendix, the details of the space transformation based on discrete Fourier transforms are documented.

a. From (x, y) space to $(k*, l*)$ space

First, reduce the dimensions from (x, y, z, t) space to (x, y) space. In most parts of the current study, the altitude of interest is 12 km, and the hours of interest are listed in the caption of Fig. 1. The simulations have periodic boundary conditions in direction x. To concentrate on the area of interest (region with active baroclinic wave and gravity wave signals), the y dimension is confined to the region between $y = 2010$ km and $y = 6000$ km. Therefore, the numbers of points along the x and y directions (N_x and N_y) are both 400, and the resolutions along the x and y directions (Δx and Δy) are both 10 km.

Following the abovementioned procedure, the zonal velocity component u is now only a function of x and y. The $(k*, l*)$ space distribution of the power spectral density based on $u(x, y)$ is defined as follows:

$$\overline{u'(x, y)u'(x, y)}(k*, l*)$$
$$= \mathrm{Re}(\mathrm{F2}[u(x, y)]\mathrm{Conj}\{\mathrm{F2}[u(x, y)]\}), \quad (A1)$$

where F2[ ] computes the two-step forward complex discrete Fourier transform along each dimension of the two-dimensional variable inside the bracket, which is normalized by the number of points along the corresponding dimension after each step. Here, F2[$u(x, y)$] transforms $u(x, y)$ from the (x, y) space with real numbers at each point into the $(k*, l*)$ space with complex numbers at each point, where zonal $k*$ and meridional $l*$ wavenumbers indicate how many waves of x-direction wavelength λ_x and y-direction wavelength λ_y fit the

length of the selected domain in the x and y direction (i.e., $|k*| = N_x\Delta x/\lambda_x$; $|l*| = N_y\Delta y/\lambda_y$), respectively. The complex conjugate of the variable is Conj{ }, and Re( ) is the real part of the variable.

Similarly, the $(k*, l*)$ space distribution of the density-weighted cospectrum based on zonal velocity component $u(x, y)$ and vertical velocity component $w(x, y)$ is defined as below:

$$\rho_0\overline{u'(x, y)w'(x, y)}(k*, l*)$$
$$= \mathrm{AVG}[\rho(x, y)]\mathrm{Re}(\mathrm{F2}[u(x, y)]\mathrm{Conj}\{\mathrm{F2}[w(x, y)]\}), \quad (A2)$$

where AVG[ ] computes the average of the variable regardless of dimensionality.

In the current study, Fig. 8 follows Eq. (A1), but the zonal velocity component is replaced by horizontal divergence; Figs. 10a–c follow Eq. (A2); Figs. 10d–f follow Eq. (A2), but the zonal velocity component is replaced by the meridional velocity component.

b. From (x, y) space to λ_H space

First, reduce the dimensions from (x, y, z, t) space to (x, y) space by following the same procedure in the first paragraph of section a of the appendix.

After the above procedure, calculate the $(k*, l*)$ space distribution of the power spectral density based on $u(x, y)$ with Eq. (A1) [i.e., $\overline{u'(x, y)u'(x, y)}(k*, l*)$]. In the $(k*, l*)$ space, the horizontal wavenumber with respect to the x direction $K^*_{H,\mathrm{wrx}}$ is defined as below:

$$K^*_{H,\mathrm{wrx}} = \sqrt{(k^*_{\mathrm{wrx}})^2 + (l^*_{\mathrm{wrx}})^2}, \quad (A3)$$

where k^*_{wrx} and l^*_{wrx}, zonal and meridional wavenumber with respect to the x direction, indicate how many waves of x-direction wavelength λ_x and y-direction wavelength λ_y fit the length of the selected domain in the x direction (i.e., $|k^*_{\mathrm{wrx}}| = N_x\Delta x/\lambda_x$; $|l^*_{\mathrm{wrx}}| = N_x\Delta x/\lambda_y$), respectively. Note that the relationships between $k*$ and k^*_{wrx}, as well as those between $l*$ and l^*_{wrx}, can be found in the below equations:

$$k^*_{\mathrm{wrx}} = k* \quad \text{and} \quad (A4)$$

$$l^*_{\mathrm{wrx}} = l*\frac{N_x\Delta x}{N_y\Delta y}. \quad (A5)$$

The one-dimensional λ_H distribution of power spectra of two-dimensional $u(x, y)$ is based on the below equation, which is the summation of the corresponding power spectral density $\overline{u'(x, y)u'(x, y)}(k*, l*)$ [Eq. (A1)] within circular shells in the entire $(k*, l*)$ space bounded by $[K^{\mathrm{int}*}_{H,\mathrm{wrx}} - (1/2)] \leq K^*_{H,\mathrm{wrx}} < [K^{\mathrm{int}*}_{H,\mathrm{wrx}} + (1/2)]$, with the

integer horizontal wavenumber with respect to the x direction $K_{H,\mathrm{wrx}}^{\mathrm{int}*}$ as the central radii of the shells:

$$E_{u(x,y)}(K_{H,\mathrm{wrx}}^{\mathrm{int}*}) = \sum_{\mathrm{C1}} \overline{u'(x,y)u'(x,y)}(k^*,l^*), \quad (A6)$$

where condition C1 represents $[K_{H,\mathrm{wrx}}^{\mathrm{int}*} - (1/2)] \leq K_{H,\mathrm{wrx}}^* < [K_{H,\mathrm{wrx}}^{\mathrm{int}*} + (1/2)]$. Equation (A6) is the same as or similar to the spectra calculations described in Errico (1985), Morss et al. (2009), Waite and Snyder (2013), Zhang et al. (2013), and Bei and Zhang (2014). In addition, the current study also computes the power spectra only within the first and third quadrant in (k^*, l^*) space (i.e., $k^*l^* > 0$), as well as those only within the second and fourth quadrant in (k^*, l^*) space (i.e., $k^*l^* < 0$). The calculations are expressed as below:

$$E_{u(x,y)}^{1,3}(K_{H,\mathrm{wrx}}^{\mathrm{int}*}) = \sum_{\mathrm{C1\,and\,C2}} \overline{u'(x,y)u'(x,y)}(k^*,l^*) \quad (A7)$$

and

$$E_{u(x,y)}^{2,4}(K_{H,\mathrm{wrx}}^{\mathrm{int}*}) = \sum_{\mathrm{C1\,and\,C3}} \overline{u'(x,y)u'(x,y)}(k^*,l^*), \quad (A8)$$

where conditions C2 and C3 represent $k^*l^* > 0$ and $k^*l^* < 0$, respectively. Finally, $E_{u(x,y)}(K_{H,\mathrm{wrx}}^{\mathrm{int}*})$, $E_{u(x,y)}^{1,3}(K_{H,\mathrm{wrx}}^{\mathrm{int}*})$, and $E_{u(x,y)}^{2,4}(K_{H,\mathrm{wrx}}^{\mathrm{int}*})$ can be converted into $E_{u(x,y)}(\lambda_H)$, $E_{u(x,y)}^{1,3}(\lambda_H)$, and $E_{u(x,y)}^{2,4}(\lambda_H)$ with the following relation:

$$K_{H,\mathrm{wrx}}^{\mathrm{int}*} = \frac{N_x \Delta x}{\lambda_H}. \quad (A9)$$

In the current study, Fig. 9a (Fig. 9b) follows Eq. (A6) [Eqs. (A7)–(A8)], but the zonal velocity component is replaced by horizontal divergence.

c. From (x, y) space to (k^*, l^*) space, back to (x, y) space

First, reduce the dimensions from (x, y, z, t) space to (x, y) space by following the same procedure in the first paragraph of section a of the appendix. After the above procedure, calculate the gravity wave–induced perturbation of $u(x, y)$ by using the bandpass filter described below:

$$u_{\mathrm{GW}}'(x,y) = \mathrm{Re}[\mathrm{B2}(\mathrm{Filter\_XY}_{(50\,\mathrm{km},600\,\mathrm{km})}\{\mathrm{F2}[u(x,y)]\})], \quad (A10)$$

where $\mathrm{Filter\_XY}_{(50\,\mathrm{km},600\,\mathrm{km})}$ modifies $\mathrm{F2}[u(x, y)]$ by only keeping those points with horizontal wavelength λ_H between 50 and 600 km in the (k^*, l^*) space (all the other points will be replaced by zero), and $\mathrm{B2}(\,)$ computes the corresponding two-step backward complex discrete Fourier transform from $\mathrm{F2}[\,]$. The (x, y) space

distribution of the density-weighted vertical flux of zonal momentum is defined as below:

$$\rho_0 \overline{u'(x,y)w'(x,y)}(x,y)$$
$$= \rho(x,y)\mathrm{sm\_XY11}[u_{\mathrm{GW}}'(x,y)w_{\mathrm{GW}}'(x,y)], \quad (A11)$$

where $\mathrm{sm\_XY11}[\,]$ computes the 11-point running average along both the x and y directions for the variable inside the bracket.

In the current study, Fig. 2 follows Eq. (A11) and Fig. 3 follows Eq. (A11), but the zonal velocity component is replaced by meridional velocity component. The calculations of the vertical gradient for the wave-induced forcing in Figs. 4b–d (as well as those calculations in Figs. 5–6) are based on the information of the fluxes in the three-dimensional (x, y, z) space (vertical resolution is interpolated into $\Delta z = 0.25$ km from the model vertical layers in this study).

d. From (x, y) space to (λ_x, y) space

First, reduce the dimensions from (x, y, z, t) space to (x, y) space by following the same procedure in the first paragraph of section a of the appendix. After the above procedure, calculate the one-dimensional density-weighted cospectrum between the zonal velocity component and vertical velocity component at each y as follows:

$$\rho_0 \overline{u'(x,y)w'(x,y)}(\lambda_x,y)$$
$$= \mathrm{AVG\_X}[\rho(x,y)]\mathrm{Cospc1\_X}[u(x,y),w(x,y)], \quad (A12)$$

where $\mathrm{AVG\_X}[\,]$ computes the average of the variable inside the bracket only along the x dimension, and $\mathrm{Cospc1\_X}[\,]$ computes the one-dimensional cospectrum between the two variables inside the bracket only along the x dimension.

In the current study, Figs. 7a–c follow Eq. (A12) and Figs. 7d–f follow Eq. (A12), but the zonal velocity component is replaced by the meridional velocity component.

e. From (x, y, t) space to (c_{px}, y) space

First, reduce the dimensions from (x, y, z, t) space to (x, y, t) space by choosing a fixed height at 12 km. In this study, WRF data are available every 1 min (i.e., $\Delta t = 1$ min), and the total time duration is 48 h (i.e., $N_t \Delta t = 48$ h), which center at the hours of interest listed in the caption of Fig. 1. The below equation shows the (k^*, y, ω^*) space distribution of the power spectral density based on the cospectrum between the two-dimensional discrete Fourier transform of zonal velocity component $u(x, y, t)$ and that of vertical velocity

component $w(x, y, t)$ within 48 h (time resolution as 1 min) at each y:

$$
\begin{aligned}
\overline{u'(x,y,t)w'(x,y,t)}(k^*, y, \omega^*) \\
= \mathrm{Re}(\mathrm{F2\_XT}[u(x,y,t)]\mathrm{Conj}\{\mathrm{F2\_XT}[w(x,y,t)]\}),
\end{aligned}
\tag{A13}
$$

where F2_XT[ ] computes the two-step forward complex discrete Fourier transform only along the x and t dimensions of the variable inside the bracket, which is normalized by the number of points along the corresponding dimension after each step. Here, $|\omega^*| = N_t \Delta t / T$, where ω^* is the temporal wavenumber, and T represents the ground-based period. In the (k^*, y, ω^*) space, the

ground-based gravity wave phase velocity along x direction c_{px} is defined as follows:

$$
c_{px} = -\frac{\omega^*}{k^*} \frac{N_x \Delta x}{N_t \Delta t}.
\tag{A14}
$$

The two-dimensional (c_{px}, y) space distribution of $\rho_0 \overline{u'w'}$ at a fixed altitude is shown in the below equation, which is based on the density-weighted summation of the corresponding power spectral density $\overline{u'(x, y, t)w'(x, y, t)}(k^*, y, \omega^*)$ [Eq. (A13)] within bands in the entire (k^*, ω^*) space at each y bounded by $[c_{px}^{\mathrm{int}} - (1/2)] \leq c_{px} < [c_{px}^{\mathrm{int}} + (1/2)]$, with the integer ground-based gravity wave phase velocity along the x direction c_{px}^{int} as the centers of the bands:

$$
\rho_0 \overline{u'(x,y,t)w'(x,y,t)}(c_{px}, y) = \mathrm{AVG\_XT}[\rho(x,y,t)] \sum_{\mathrm{C4, C5, and\ C6}} \overline{u'(x,y,t)w'(x,y,t)}(k^*, y, \omega^*),
\tag{A15}
$$

where AVG_XT[ ] computes the average of the variable inside the bracket only along the x and t dimensions; condition C4 represents $[c_{px}^{\mathrm{int}} - (1/2)] \leq c_{px} < [c_{px}^{\mathrm{int}} + (1/2)]$ (i.e., the resolution of c_{px} is $1\,\mathrm{m\,s^{-1}}$ in the current study); condition C5 represents $50 \leq \lambda_x \leq 800\,\mathrm{km}$ (i.e., large-scale baroclinic wave signals will be largely filtered); and condition C6 represents $T \geq 5\,\mathrm{min}$. Equation (A15) is similar to those calculations in Lee (1997) and Chun et al. (2005).

In the current study, Fig. 11 follows Eq. (A15).

f. From (x, y, t) space to (C_{HP_x}, C_{HP_y}) space

First, reduce the dimensions from (x, y, z, t) space to (x, y, t) space by choosing a fixed height at 12 km. In this study, WRF data are available every 1 min (i.e., $\Delta t = 1$ min), and the total time duration is 48 h (i.e., $N_t \Delta t = 48$ h), which centers at the hours of interest listed in the caption of Fig. 1. The below equation shows the (k^*, l^*, ω^*) space distribution of the power spectral density based on the cospectrum between the three-dimensional discrete Fourier transform of zonal velocity component $u(x, y, t)$ and that of the vertical velocity component $w(x, y, t)$ within 48 h (time resolution as 1 min):

$$
\begin{aligned}
\overline{u'(x,y,t)w'(x,y,t)}(k^*, l^*, \omega^*) = \mathrm{Re}(\mathrm{F3\_XYT}[u'_{\mathrm{GW}}(x,y,t)] \\
\times \mathrm{Conj}\{\mathrm{F3\_XYT}[w'_{\mathrm{GW}}(x,y,t)]\}),
\end{aligned}
\tag{A16}
$$

where F3_XYT[ ] computes the three-step forward complex discrete Fourier transform only along x, y, and t dimensions of the variable inside the bracket, which is normalized by the number of points along the

corresponding dimension after each step. In the (k^*, l^*, ω^*) space, the ground-based horizontal gravity wave phase velocity (C_{HP_x}, C_{HP_y}) is defined as follows:

$$
(C_{HP\_x}, C_{HP\_y}) = \left[-\frac{\omega^*}{(K_{H,\mathrm{wrx}}^*)^2} \frac{N_x \Delta x}{N_t \Delta t} \right] \times (k_{\mathrm{wrx}}^*, l_{\mathrm{wrx}}^*).
\tag{A17}
$$

The two-dimensional (C_{HP_x}, C_{HP_y}) space distribution of $\rho_0 \overline{u'w'}$ at a fixed altitude is shown in the below equation, which is based on the density-weighted summation of the corresponding power spectral density $\overline{u'(x, y, t)w'(x, y, t)}(k^*, l^*, \omega^*)$ [Eq. (A16)] within volumes in the entire (k^*, l^*, ω^*) space bounded by $[C_{HP\_x}^{\mathrm{int}} - (1/2)] \leq C_{HP\_x} < [C_{HP\_x}^{\mathrm{int}} + (1/2)]$ and $[C_{HP\_y}^{\mathrm{int}} - (1/2)] \leq C_{HP\_y} < [C_{HP\_y}^{\mathrm{int}} + (1/2)]$, with $C_{HP\_x}^{\mathrm{int}}$ ($C_{HP\_y}^{\mathrm{int}}$) as the x (y) component of integer ground-based horizontal gravity wave phase velocity,

$$
\begin{aligned}
\rho_0 \overline{u'(x,y,t)w'(x,y,t)}(C_{HP\_x}, C_{HP\_y}) = \mathrm{AVG\_XYT}[\rho(x,y,t)] \\
\times \sum_{\mathrm{C7\ and\ C8}} \overline{u'(x,y,t)w'(x,y,t)}(k^*, l^*, \omega^*),
\end{aligned}
\tag{A18}
$$

where AVG_XYT[ ] computes the average of the variable inside the bracket only along x, y, and t dimensions, and conditions C7 and C8 represent $[C_{HP\_x}^{\mathrm{int}} - (1/2)] \leq C_{HP\_x} < [C_{HP\_x}^{\mathrm{int}} + (1/2)]$ and $[C_{HP\_y}^{\mathrm{int}} - (1/2)] \leq C_{HP\_y} < [C_{HP\_y}^{\mathrm{int}} + (1/2)]$, respectively (i.e., the resolutions of both C_{HP_x} and C_{HP_y} are $1\,\mathrm{m\,s^{-1}}$ in the current study). Equation (A18) is similar to those calculations in Kim

et al. (2009), Alexander et al. (2004), Stephan and Alexander (2014), and Kim et al. (2014). Therefore, this method is generally consistent with many other studies, although there may be some minor differences. First, the definition for gravity wave component may be different (also see the discussion in the first paragraph of section 3). Second, other studies may sum up the flux/energy within a certain small range of the magnitudes and angles of the horizontal phase velocities, while the current study uses a certain small range of the x and y components of the horizontal phase velocities.

In the current study, Fig. 13 follows Eq. (A18); Figs. 14a–c (Figs. 14d–f) follow Eq. (A18), but u'_{GW} and w'_{GW} in Eq. (A16) are replaced by short-scale (medium scale) perturbations of the zonal velocity component and vertical velocity component with horizontal wavelength between 50 and 200 km (between 200 and 600 km) by modifying Eq. (A10); Figs. 15a–c (Figs. 15d–f) follow Eq. (A18), but it is calculated within the northern (southern) purple box in Fig. 2.

REFERENCES

Achatz, U., R. Klein, and F. Senf, 2010: Gravity waves, scale asymptotics and the pseudo-incompressible equations. *J. Fluid Mech.*, **663**, 120–147, doi:10.1017/S0022112010003411.

Alexander, M. J., and T. J. Dunkerton, 1999: A spectral parameterization of mean-flow forcing due to breaking gravity waves. *J. Atmos. Sci.*, **56**, 4167–4182, doi:10.1175/1520-0469(1999)056<4167:ASPOMF>2.0.CO;2.

——, J. R. Holton, and D. R. Durran, 1995: The gravity wave response above deep convection in a squall line simulation. *J. Atmos. Sci.*, **52**, 2212–2226, doi:10.1175/1520-0469(1995)052<2212:TGWRAD>2.0.CO;2.

——, P. T. May, and J. H. Beres, 2004: Gravity waves generated by convection in the Darwin area during the Darwin Area Wave Experiment. *J. Geophys. Res.*, **109**, D20S04, doi:10.1029/2004JD004729.

——, and Coauthors, 2010: Recent developments in gravity-wave effects in climate models and the global distribution of gravity-wave momentum flux from observations and models. *Quart. J. Roy. Meteor. Soc.*, **136**, 1103–1124, doi:10.1002/qj.637.

Andrews, D., J. Holton, and C. Leovy, 1987: *Middle Atmosphere Dynamics*. International Geophysics Series, Vol. 40, Academic Press, 489 pp.

Bei, N., and F. Zhang, 2014: Mesoscale predictability of moist baroclinic waves: Variable and scale-dependent error growth. *Adv. Atmos. Sci.*, **31**, 995–1008, doi:10.1007/s00376-014-3191-7.

Beres, J. H., 2004: Gravity wave generation by a three-dimensional thermal forcing. *J. Atmos. Sci.*, **61**, 1805–1815, doi:10.1175/1520-0469(2004)061<1805:GWGBAT>2.0.CO;2.

——, M. Alexander, and J. Holton, 2004: A method of specifying the gravity wave spectrum above convection based on latent heating properties and background wind. *J. Atmos. Sci.*, **61**, 324–337, doi:10.1175/1520-0469(2004)061<0324:AMOSTG>2.0.CO;2.

——, R. R. Garcia, B. Boville, and F. Sassi, 2005: Implementation of a gravity wave source spectrum parameterization dependent on the properties of convection in the Whole Atmosphere Community Climate Model (WACCM). *J. Geophys. Res.*, **110**, D10108, doi:10.1029/2004JD005504.

Bretherton, F., 1966: The propagation of groups of internal gravity waves in a shear flow. *Quart. J. Roy. Meteor. Soc.*, **92**, 466–480, doi:10.1002/qj.49709239403.

Charron, M., and E. Manzini, 2002: Gravity waves from fronts: Parameterization and middle atmosphere response in a general circulation model. *J. Atmos. Sci.*, **59**, 923–941, doi:10.1175/1520-0469(2002)059<0923:GWFFPA>2.0.CO;2.

Choi, H.-J., and H.-Y. Chun, 2011: Momentum flux spectrum of convective gravity waves. Part I: An update of a parameterization using mesoscale simulations. *J. Atmos. Sci.*, **68**, 739–759, doi:10.1175/2010JAS3552.1.

Chun, H.-Y., I.-S. Song, and T. Horinouchi, 2005: Momentum flux spectrum of convectively forced gravity waves: Can diabatic forcing be a proxy for convective forcing? *J. Atmos. Sci.*, **62**, 4113–4120, doi:10.1175/JAS3610.1.

Clark, T. L., T. Hauf, and J. P. Kuettner, 1986: Convectively forced internal gravity waves: Results from two-dimensional numerical experiments. *Quart. J. Roy. Meteor. Soc.*, **112**, 899–925, doi:10.1002/qj.49711247402.

de la Cámara, A., and F. Lott, 2015: A parameterization of gravity waves emitted by fronts and jets. *Geophys. Res. Lett.*, **42**, 2071–2078, doi:10.1002/2015GL063298.

Dunkerton, T. J., and N. Butchart, 1984: Propagation and selective transmission of internal gravity waves in a sudden warming. *J. Atmos. Sci.*, **41**, 1443–1460, doi:10.1175/1520-0469(1984)041<1443:PASTOI>2.0.CO;2.

Durran, D. R., 1986: Mountain waves. *Mesoscale Meteorology and Forecasting*. P. S. Ray, Ed., Amer. Meteor. Soc., 472–492.

——, 1990: Mountain waves and downslope winds. *Atmospheric Processes over Complex Terrain*, *Meteor. Monogr.*, No. 45, Amer. Meteor. Soc., 59–81.

——, 2003: Lee waves and mountain waves. *Encyclopedia of Atmospheric Sciences*. J. R. Holton, J. Pyle, and J. A. Curry, Eds., Elsevier Science, 1161–1169.

Eliassen, A., and E. Palm, 1960: On the transfer of energy in stationary mountain waves. *Geofys. Publ.*, **22** (3), 1–23.

Errico, R. M., 1985: Spectra computed from a limited area grid. *Mon. Wea. Rev.*, **113**, 1554–1562, doi:10.1175/1520-0493(1985)113<1554:SCFALA>2.0.CO;2.

Fovell, R., D. Durran, and J. R. Holton, 1992: Numerical simulations of convectively generated stratospheric gravity waves. *J. Atmos. Sci.*, **49**, 1427–1442, doi:10.1175/1520-0469(1992)049<1427:NSOCGS>2.0.CO;2.

Fritts, D. C., and M. J. Alexander, 2003: Gravity wave dynamics and effects in the middle atmosphere. *Rev. Geophys.*, **41**, 1003, doi:10.1029/2001RG000106.

Geller, M. A., and Coauthors, 2011: New gravity wave treatments for GISS climate models. *J. Climate*, **24**, 3989–4002, doi:10.1175/2011JCLI4013.1.

——, and Coauthors, 2013: A comparison between gravity wave omentum fluxes in observations and limate models. *J. Climate*, **26**, 6383–6405, doi:10.1175/JCLI-D-12-00545.1.

Griffiths, M., and M. J. Reeder, 1996: Stratospheric inertia–gravity waves generated in a numerical model of frontogenesis. I: Model solutions. *Quart. J. Roy. Meteor. Soc.*, **122**, 1153–1174, doi:10.1002/qj.49712253307.

Grimshaw, R., 1975: Internal gravity waves: Critical layer absorption in a rotating fluid. *J. Fluid Mech.*, **70**, 287–304, doi:10.1017/S0022112075002030.

Guest, F. M., M. J. Reeder, C. J. Marks, and D. J. Karoly, 2000: Inertia–gravity waves observed in the lower stratosphere over

Macquarie Island. *J. Atmos. Sci.*, **57**, 737–752, doi:10.1175/1520-0469(2000)057<0737:IGWOIT>2.0.CO;2.

Haynes, P., 2005: Stratospheric dynamics. *Annu. Rev. Fluid Mech.*, **37**, 263–293, doi:10.1146/annurev.fluid.37.061903.175710.

Hertzog, A., and Coauthors, 2007: Stratéole/Vorcore—Long-duration, superpressure balloons to study the Antarctic lower stratosphere during the 2005 winter. *J. Atmos. Oceanic Technol.*, **24**, 2048–2061, doi:10.1175/2007JTECHA948.1.

——, G. Boccara, R. A. Vincent, F. Vial, and P. Cocquerez, 2008: Estimation of gravity wave momentum flux and phase speeds from quasi-Lagrangian stratospheric balloon flights. Part II: Results from the Vorcore campaign in Antarctica. *J. Atmos. Sci.*, **65**, 3056–3070, doi:10.1175/2008JAS2710.1.

Holton, J. R., 1982: The role of gravity wave induced drag and diffusion in the momentum budget of the mesosphere. *J. Atmos. Sci.*, **39**, 791–799, doi:10.1175/1520-0469(1982)039<0791:TROGWI>2.0.CO;2.

——, 1983: The influence of gravity wave breaking on the general circulation of the middle atmosphere. *J. Atmos. Sci.*, **40**, 2497–2507, doi:10.1175/1520-0469(1983)040<2497:TIOGWB>2.0.CO;2.

——, P. H. Haynes, M. E. McIntyre, A. R. Douglass, R. B. Road, and L. Pfister, 1995: Stratosphere–troposphere exchange. *Rev. Geophys.*, **33**, 403–439, doi:10.1029/95RG02097.

Jewett, B. F., M. K. Ramamurthy, and R. M. Rauber, 2003: Origin, evolution, and finescale structure of the St. Valentine's Day mesoscale gravity wave observed during STORM-FEST. Part III: Gravity wave genesis and the role of evaporation. *Mon. Wea. Rev.*, **131**, 617–633, doi:10.1175/1520-0493(2003)131<0617:OEAFSO>2.0.CO;2.

Kim, S. H., H.-Y. Chun, and W. Jang, 2014: Horizontal divergence of typhoon-generated gravity waves in the upper troposphere and lower stratosphere (UTLS) and its influence on typhoon evolution. *Atmos. Chem. Phys.*, **14**, 3175–3182, doi:10.5194/acp-14-3175-2014.

Kim, S.-Y., and H.-Y. Chun, 2010: Stratospheric gravity waves generated by Typhoon Saomai (2006): Numerical modeling in a moving frame following the typhoon. *J. Atmos. Sci.*, **67**, 3617–3636, doi:10.1175/2010JAS3374.1.

——, ——, and D. L. Wu, 2009: A study on stratospheric gravity waves generated by Typhoon Ewiniar: Numerical simulations and satellite observations. *J. Geophys. Res.*, **114**, D22104, doi:10.1029/2009JD011971.

Kim, Y.-H., H.-Y. Chun, S.-H. Park, I.-S. Song, and H.-J. Choi, 2016: Characteristics of gravity waves generated in the jet-front system in a baroclinic instability simulation. *Atmos. Chem. Phys.*, **16**, 4799–4815, doi:10.5194/acp-16-4799-2016.

Kim, Y.-J., S. D. Eckermann, and H. Y. Chun, 2003: An overview of the past, present and future of gravity-wave drag parametrization for numerical climate and weather prediction models. *Atmos.–Ocean*, **41**, 65–98, doi:10.3137/ao.410105.

Koch, S. E., and P. B. Dorian, 1988: A mesoscale gravity wave event observed during CCOPE. Part III: Wave environment and probable source mechanisms. *Mon. Wea. Rev.*, **116**, 2570–2592, doi:10.1175/1520-0493(1988)116<2570:AMGWEO>2.0.CO;2.

——, and Coauthors, 2005: Turbulence and gravity waves within an upper-level front. *J. Atmos. Sci.*, **62**, 3885–3908, doi:10.1175/JAS3574.1.

Lane, T. P., and F. Zhang, 2011: Coupling between gravity waves and tropical convection at mesoscales. *J. Atmos. Sci.*, **68**, 2582–2598, doi:10.1175/2011JAS3577.1.

——, M. J. Reeder, and T. L. Clark, 2001: Numerical modeling of gravity wave generation by deep tropical convection. *J. Atmos.*

Sci., **58**, 1249–1274, doi:10.1175/1520-0469(2001)058<1249:NMOGWG>2.0.CO;2.

——, J. D. Doyle, R. Plougonven, M. A. Shapiro, and R. D. Sharman, 2004: Observations and numerical simulations of inertia–gravity waves and shearing instabilities in the vicinity of a jet stream. *J. Atmos. Sci.*, **61**, 2692–2706, doi:10.1175/JAS3305.1.

Lee, S., 1997: Maintenance of multiple jets in a baroclinic flow. *J. Atmos. Sci.*, **54**, 1726–1738, doi:10.1175/1520-0469(1997)054<1726:MOMJIA>2.0.CO;2.

Lin, Y., and F. Zhang, 2008: Tracking gravity waves in baroclinic jet-front systems. *J. Atmos. Sci.*, **65**, 2402–2415, doi:10.1175/2007JAS2482.1.

Lindzen, R. S., 1981: Turbulence and stress owing to gravity wave and tidal breakdown. *J. Geophys. Res.*, **86**, 9707–9714, doi:10.1029/JC086iC10p09707.

——, 1990: *Dynamics in Atmospheric Physics*. Cambridge University Press, 320 pp.

Lott, F., 1999: Alleviation of stationary biases in a GCM through a mountain drag parameterization scheme and a simple representation of mountain lift forces. *Mon. Wea. Rev.*, **127**, 788–801, doi:10.1175/1520-0493(1999)127<0788:AOSBIA>2.0.CO;2.

——, and M. J. Miller, 1997: A new subgrid-scale orographic gravity wave parameterization: Its formulation and testing. *Quart. J. Roy. Meteor. Soc.*, **123**, 101–127, doi:10.1002/qj.49712353704.

McFarlane, N. A., 1987: The effect of orographically excited gravity wave drag on the general circulation of the lower stratosphere and troposphere. *J. Atmos. Sci.*, **44**, 1775–1800, doi:10.1175/1520-0469(1987)044<1775:TEOOEG>2.0.CO;2.

Mirzaei, M., C. Zülicke, A. R. Mohebalhojeh, F. Ahmadi-Givi, and R. Plougonven, 2014: Structure, energy, and parameterization of inertia–gravity waves in dry and moist simulations of a baroclinic wave life cycle. *J. Atmos. Sci.*, **71**, 2390–2414, doi:10.1175/JAS-D-13-075.1.

Miyahara, S., 2006: A three-dimensional wave activity flux applicable to inertio-gravity waves. *SOLA*, **2**, 108–111, doi:10.2151/sola.2006-028.

Morss, R. E., C. Snyder, and R. Rotunno, 2009: Spectra, spatial scales, and predictability in a quasigeostrophic model. *J. Atmos. Sci.*, **66**, 3115–3130, doi:10.1175/2009JAS3057.1.

Müller, P., 1976: On the diffusion of momentum and mass by internal gravity waves. *J. Fluid Mech.*, **77**, 789–823, doi:10.1017/S0022112076002899.

O'Sullivan, D., and T. J. Dunkerton, 1995: Generation of inertia–gravity waves in a simulated life cycle of baroclinic instability. *J. Atmos. Sci.*, **52**, 3695–3716, doi:10.1175/1520-0469(1995)052<3695:GOIWIA>2.0.CO;2.

Palmer, T., G. Shutts, and R. Swinbank, 1986: Alleviation of systematic westerly bias in general circulation and numerical weather prediction models through an orographic gravity wave drag parameterization. *Quart. J. Roy. Meteor. Soc.*, **112**, 1001–1039, doi:10.1002/qj.49711247406.

Park, S.-H., J. B. Klemp, and W. C. Skamarock, 2014: A comparison of mesh refinement in the global MPAS-A and WRF models using an idealized normal-mode baroclinic wave simulation. *Mon. Wea. Rev.*, **142**, 3614–3634, doi:10.1175/MWR-D-14-00004.1.

Pavelin, E., J. A. Whiteway, and G. Vaughan, 2001: Observation of gravity wave generation and breaking in the lowermost stratosphere. *J. Geophys. Res.*, **106**, 5173–5179, doi:10.1029/2000JD900480.

Plougonven, R., and C. Snyder, 2005: Gravity waves excited by jets: Propagation versus generation. *Geophys. Res. Lett.*, **32**, L18802, doi:10.1029/2005GL023730.

——, and ——, 2007: Inertia–gravity waves spontaneously generated by jets and fronts. Part I: Different baroclinic life cycles. *J. Atmos. Sci.*, **64**, 2502–2520, doi:10.1175/JAS3953.1.

——, and F. Zhang, 2014: Internal gravity waves from atmospheric jets and fronts. *Rev. Geophys.*, **52**, doi:10.1002/2012RG000419.

——, A. Hertzog, and M. J. Alexander, 2015: Case studies of nonorographic gravity waves over the Southern Ocean emphasize the role of moisture. *J. Geophys. Res. Atmos.*, **120**, 1278–1299, doi:10.1002/2014JD022332.

Preusse, P., M. Ern, P. Bechtold, S. D. Eckermann, S. Kalisch, Q. T. Trinh, and M. Riese, 2014: Characteristics of gravity waves resolved by ECMWF. *Atmos. Chem. Phys.*, **14**, 10 483–10 508, doi:10.5194/acp-14-10483-2014.

Queney, P., 1948: The problem of air flow over mountains: A summary of theoretical studies. *Bull. Amer. Meteor. Soc.*, **29**, 16–26.

Richter, J. H., F. Sassi, and R. R. Garcia, 2010: Toward a physically based gravity wave source parameterization in a general circulation model. *J. Atmos. Sci.*, **67**, 136–156, doi:10.1175/2009JAS3112.1.

Rind, D., R. Suozzo, N. Balachandran, A. Lacis, and G. Russell, 1988: The GISS global climate-middle atmosphere model. Part I: Model structure and climatology. *J. Atmos. Sci.*, **45**, 329–370, doi:10.1175/1520-0469(1988)045<0329:TGGCMA>2.0.CO;2.

Scinocca, J. F., and N. A. McFarlane, 2000: The parameterization of drag induced by stratified flow over anisotropic orography. *Quart. J. Roy. Meteor. Soc.*, **126**, 2353–2393, doi:10.1002/qj.49712656802.

Shapiro, M. A., 1980: Turbulent mixing within tropopause folds as a mechanism for the exchange of chemical constituents between the stratosphere and troposphere. *J. Atmos. Sci.*, **37**, 994–1004, doi:10.1175/1520-0469(1980)037<0994:TMWTFA>2.0.CO;2.

Shutts, G. J., and S. B. Vosper, 2011: Stratospheric gravity waves revealed in NWP model forecasts. *Quart. J. Roy. Meteor. Soc.*, **137**, 303–317, doi:10.1002/qj.763.

Skamarock, W. C., and Coauthors, 2008: A description of the Advanced Research WRF version 3. NCAR Tech. Note NCAR/TN-475+STR, 113 pp., doi:10.5065/D68S4MVH.

Smith, R. B., 1980: Linear theory of stratified hydrostatic flow past an isolated mountain. *Tellus*, **32A**, 348–364, doi:10.1111/j.2153-3490.1980.tb00962.x.

——, 1990: Why can't stably stratified air rise over high ground? *Atmospheric Processes over Complex Terrain*, *Meteor. Monogr.*, No. 23, Amer. Met. Soc., 105–107.

Snyder, C., W. C. Skamarock, and R. Rotunno, 1993: Frontal dynamics near and following frontal collapse. *J. Atmos. Sci.*, **50**, 3194–3212, doi:10.1175/1520-0469(1993)050<3194:FDNAFF>2.0.CO;2.

Song, I.-S., and H.-Y. Chun, 2005: Momentum flux spectrum of convectively forced internal gravity waves and its application to gravity wave drag parameterization. Part I: Theory. *J. Atmos. Sci.*, **62**, 107–124, doi:10.1175/JAS-3363.1.

——, and ——, 2008: A Lagrangian spectral parameterization of gravity wave drag induced by cumulus convection. *J. Atmos. Sci.*, **65**, 1204–1224, doi:10.1175/2007JAS2369.1.

Stensrud, D. J., 2007: *Parameterization Schemes: Keys to Understanding Numerical Weather Prediction Models*. Cambridge University Press, 480 pp.

Stephan, C., and M. J. Alexander, 2014: Summer season squall-line simulations: Sensitivity of gravity waves to physics parameterization and implications for their parameterization in global climate models. *J. Atmos. Sci.*, **71**, 3376–3391, doi:10.1175/JAS-D-13-0380.1.

Tan, Z. M., F. Zhang, R. Rotunno, and C. Snyder, 2004: Mesoscale predictability of moist baroclinic waves: Experiments with parameterized convection. *J. Atmos. Sci.*, **61**, 1794–1804, doi:10.1175/1520-0469(2004)061<1794:MPOMBW>2.0.CO;2; Corrigendum, **65**, 1479, doi:10.1175/2007JAS2715.1.

Uccellini, L. W., and S. E. Koch, 1987: The synoptic setting and possible source mechanisms for mesoscale gravity wave events. *Mon. Wea. Rev.*, **115**, 721–729, doi:10.1175/1520-0493(1987)115<0721:TSSAPE>2.0.CO;2.

Waite, M. L., and C. Snyder, 2013: Mesoscale energy spectra of moist baroclinic waves. *J. Atmos. Sci.*, **70**, 1242–1256, doi:10.1175/JAS-D-11-0347.1.

Wang, S., and F. Zhang, 2007: Sensitivity of mesoscale gravity waves to the baroclinicity of jet–front systems. *Mon. Wea. Rev.*, **135**, 670–688, doi:10.1175/MWR3314.1.

Warner, C. D., and M. E. McIntyre, 2001: An ultrasimple spectral parameterization for nonorographic gravity waves. *J. Atmos. Sci.*, **58**, 1837–1857, doi:10.1175/1520-0469(2001)058<1837:AUSPFN>2.0.CO;2.

Wei, J., and F. Zhang, 2014: Mesoscale gravity waves in moist baroclinic jet–front systems. *J. Atmos. Sci.*, **71**, 929–952, doi:10.1175/JAS-D-13-0171.1.

——, and ——, 2015: Tracking gravity waves in moist baroclinic jet–front systems. *J. Adv. Model. Earth Syst.*, **7**, 67–91, doi:10.1002/2014MS000395.

Zhang, F., 2004: Generation of mesoscale gravity waves in the upper-tropospheric jet–front systems. *J. Atmos. Sci.*, **61**, 440–457, doi:10.1175/1520-0469(2004)061<0440:GOMGWI>2.0.CO;2.

——, S. E. Koch, C. A. Davis, and M. L. Kaplan, 2001: Wavelet analysis and the governing dynamics of a large-amplitude gravity wave event along the East Coast of the United States. *Quart. J. Roy. Meteor. Soc.*, **127**, 2209–2245, doi:10.1002/qj.49712757702.

——, M. Zhang, J. Wei, and S. Wang, 2013: Month-long simulations of gravity waves over North America and North Atlantic in comparison with satellite observations. *Acta Meteor. Sin.*, **27**, 446–454, doi:10.1007/s13351-013-0301-x.

——, J. Wei, M. Zhang, K. P. Bowman, L. L. Pan, E. Atlas, and S. C. Wofsy, 2015: Aircraft measurements of gravity waves in the upper troposphere and lower stratosphere during the START08 field experiment. *Atmos. Chem. Phys.*, **15**, 7667–7684, doi:10.5194/acp-15-7667-2015.